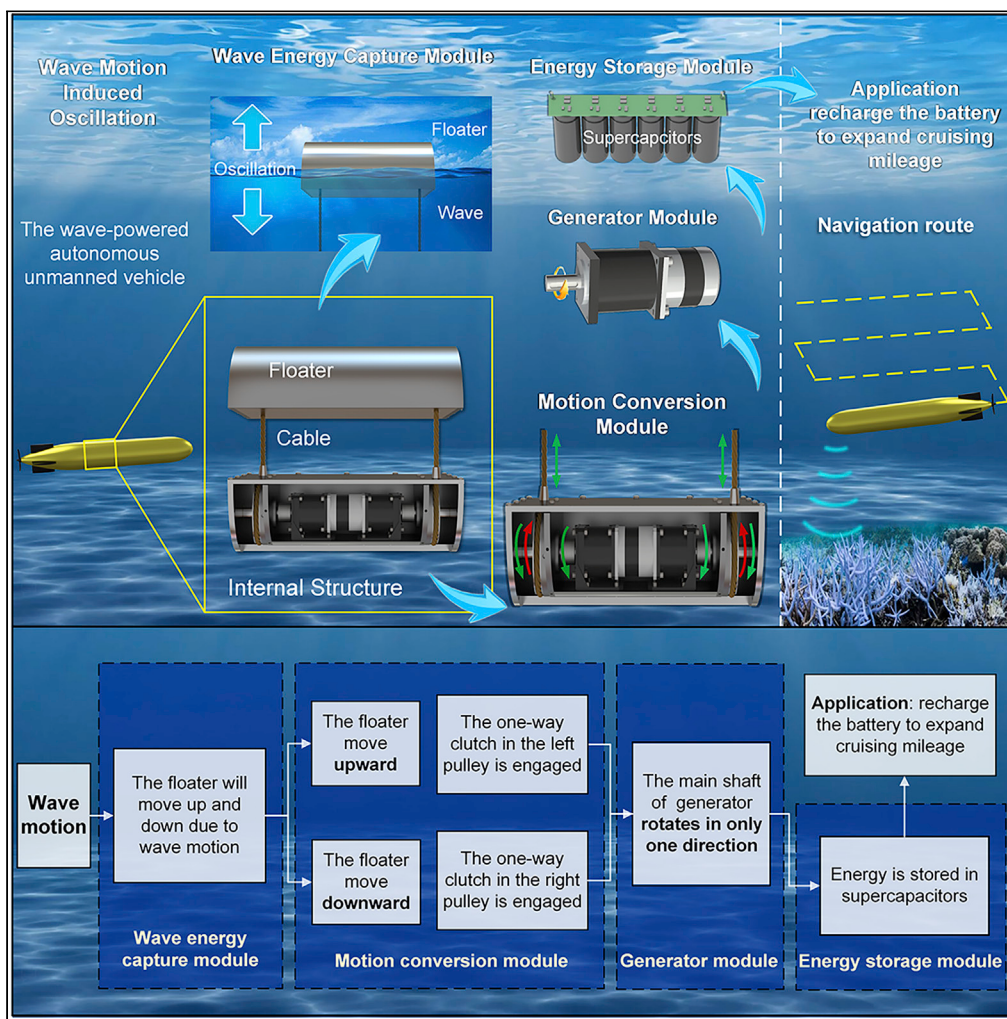


## Article

## An extended-range wave-powered autonomous underwater vehicle applied to underwater wireless sensor networks



Hai Li, Xiaoping Wu, Zutao Zhang, ..., Dabing Luo, Ammar Ahmed, Yongsheng Xu

ztt@sjtu.edu.cn (Z.Z.)  
yjpan@sjtu.edu.cn (Y.P.)

**Highlights**

An extended-range wave-powered autonomous underwater vehicle (WPAUV) is proposed

The mechanical efficiency distributes from 20.41% to 81.56%

Ambient wave energy is harvested to recharge the battery or power auxiliary devices

The results are prolific for expanding the cruising mileage

Li et al., iScience 25, 104738  
August 19, 2022 © 2022 The Authors.

<https://doi.org/10.1016/j.isci.2022.104738>



## Article

# An extended-range wave-powered autonomous underwater vehicle applied to underwater wireless sensor networks

Hai Li,<sup>1,2</sup> Xiaoping Wu,<sup>1</sup> Zutao Zhang,<sup>1,5,\*</sup> Xing Tan,<sup>1,2</sup> Yajia Pan,<sup>1,\*</sup> Chutian Dai,<sup>1,2</sup> Dabing Luo,<sup>1</sup> Ammar Ahmed,<sup>3</sup> and Yongsheng Xu<sup>4</sup>

## SUMMARY

The autonomous underwater vehicle has widespread applications in marine resource exploration, seabed search and rescue, underwater military reconnaissance, and marine environmental monitoring. Owing to the limited battery capacity, autonomous underwater vehicles usually only operate for several hours or days at a time. This article presents an extended-range wave-powered autonomous underwater vehicle (WPAUV) for underwater wireless sensor networks. Through theoretical analysis, simulation, dry and field experiments, the power generation performance of the extended-range WPAUV was evaluated. Under different wave amplitudes and wave frequencies, the mechanical efficiency of the extended-range WPAUV ranges from 20.41% to 81.56%. The average efficiency is 45.35%. In the field experiments, under calm ocean conditions, the maximum instantaneous power can reach 67.74W with an average of 10.18W. This high performance manifests that the extended-range WPAUV can effectively scavenge wave energy and converts it into electrical energy for expanding the cruising mileage.

## INTRODUCTION

Autonomous underwater vehicles (AUVs) have widespread applications in marine resource exploration, seabed search and rescue, underwater military reconnaissance, and marine environmental monitoring. The AUV does not have an umbilical cord cable to connect to the support vessel, so it can perform various tasks autonomously in a larger area. Owing to size and quality restrictions, the battery capacity is limited, which results in the AUVs only operating for several hours or days at a time (Townsend and Shenoi, 2016). In order to increase the navigation time, some researchers propose many measures to resolve the power supply of AUVs, including the use of batteries with high energy density (Han et al., 2020), the development of battery management systems (Chin et al., 2019), path planning (Niu et al., 2020). Han et al. proposed a portable fuel cell with a nominal power of 31.5W at 12V (Han et al., 2020). This fuel cell is suitable for AUVs because its energy density is twice that of traditional energy storage systems. Chin et al. proposed a smart battery management system that can perform active battery balancing and state of charge (SOC) estimation for underwater unmanned vehicles in real-time (Chin et al., 2019). Niu et al. proposed a novel energy-efficient path planning algorithm is proposed to solve the strict energy limitation of AUVs (Niu et al., 2020). Moreover, the flexibility and practicability of the proposed algorithm are verified by the ocean current and coastline databases. For AUVs, these methods reduce energy consumption and improve navigation time to a certain extent. In order to fundamentally solve the energy supply of AUVs, it is necessary to introduce new sources of energy.

In recent years, the harvesting of environmental energy has gradually become a research hotspot because of its simple, renewable, and pollution-free advantages. With the development of these renewable energy sources, some researchers have conducted some investigations, including the seasonal challenges of the renewable energy-driven grid (Abido et al., 2022), the impact of renewable energy on hydropower operation (Gøtske and Victoria, 2021), and the economics of renewable energy production-transmission pathways (DeSantis et al., 2021). Similarly, many kinds of environmental energy can be used in the working environment of AUVs. Considering this, some researchers proposed harvesting environmental energy to provide auxiliary power for the continuous operation of the AUVs. The energy that can be harvested and utilized

<sup>1</sup>School of Mechanical Engineering, Southwest Jiaotong University, Chengdu 610031, P. R. China

<sup>2</sup>Yibin Research Institute, Southwest Jiaotong University, Yibin 644000, P.R. China

<sup>3</sup>School of Mechanical Engineering, Northwestern Polytechnical University, Xi'an 710072, PR China

<sup>4</sup>School of Design and Art, Southwest Jiaotong University, Chengdu 610031, P. R. China

<sup>5</sup>Lead contact

\*Correspondence:  
[ztt@swjtu.edu.cn](mailto:ztt@swjtu.edu.cn) (Z.Z.),  
[yjpan@swjtu.edu.cn](mailto:yjpan@swjtu.edu.cn) (Y.P.)

<https://doi.org/10.1016/j.isci.2022.104738>



includes solar energy (Röhr et al., 2020), ocean thermal energy (Falcão Carneiro and Gomes de Almeida, 2018), ocean current energy (Xupeng et al., 2020), and wave energy (Townsend, 2016; Bracco et al., 2011; Fenucci et al., 2016). Röhr et al. explored the use of solar cells in AUVs. The research results show that when the power density is greater than  $5 \text{ mW/cm}^2$ , the efficiency of underwater solar cells in shallow water and deep water is 55 and 65%, respectively (Röhr et al., 2020). However, solar cells cannot generate enough electricity at night and on cloudy or rainy days. Meanwhile, solar panels usually require a larger area to install, which will increase the volume of AUVs to a certain extent. Falcão et al. proposed to obtain energy from the ocean temperature gradient to power AUVs. Moreover, each storage material was simulated to determine the design parameters (Falcão Carneiro and Gomes de Almeida, 2018). Although this method is feasible, it does not consider the increased weight of the thermoelectric generator and storage material. Han et al. proposed a distributed ocean current power generation scheme, and the feasibility was verified by simulation results and a prototype (Xupeng et al., 2020). Ocean current turbines require a mooring system fixed on the seabed, which is unsuitable for AUVs with a wide working range. As the highest-grade marine energy, wave energy seems to be more worthy of acquisition and application. Townsend et al. used a gimballed flywheel installed inside an AUV to harvest wave energy. A series of conventional wave test results proved that the peak power of the prototype is 8W under the test conditions (Townsend, 2016). Bracco et al. designed an inertial wave energy harvester and optimized the float shape to improve energy conversion efficiency. After the float shape is optimized, the energy absorbed by the harvester is increased by two times (Bracco et al., 2011). Ferrucci et al. manufactured a prototype of wave-powered AUV for marine exploration. The sea experiment results show that the prototype can continuously generate voltage peaks from wave motion in moderate sea conditions (Fenucci et al., 2016). Bowker et al. proposed a Flapping Energy Utilization and Recovery System to propel long-endurance Autonomous Surface Vehicles (Bowker et al., 2015). The results show that a maximum power of nearly 4W and an average power of 1W can be obtained.

Wave energy refers to the kinetic and potential energy of waves formed by wind on the ocean's surface, whose annual power potential is about 8000–80000 TWh (Khan et al., 2017). The energy density of wave energy is 2–3  $\text{kW/m}^2$ , which is 5 times that of wind energy and 15–20 times that of solar energy (Khan et al., 2017). All-day availability and predictability of wave energy are two other advantages compared to other marine renewable energy sources (Younesian and Alam, 2017). Therefore, ocean wave energy, as a kind of renewable clean energy with abundant reserves and wide distribution, provides a feasible approach to solve the power supply of AUV. Meanwhile, based on different energy harvesting methods, various wave energy conversion systems are proposed. According to the working principle, recent literature identifies three categories of wave energy harvesters (Falcão, 2010): oscillating water column systems, overtopping systems, oscillating body systems.

The oscillating water column system mainly consists of a submerged concrete or steel structure, which opens below the water surface and whose cavity above the water surface is filled with air. The up and down movement of the waves changes the pressure of the air inside and outside the cavity, thereby driving the air turbine to the top of the cavity. In this way, wave energy is converted into mechanical energy and then into electrical energy. Zhou et al. proposed a mushroom-shaped oscillating water column system not restricted by wave direction and coastline geographic conditions (Zhou et al., 2018). The analysis results showed that a shell with a lower draft and wider chamber could obtain a wider frequency bandwidth. Lopez et al. considered the variability of wave resources, which is often ignored when analyzing the performance of wave energy converters (López et al., 2020). A case study found that the variability of wave sources exceeded 20% in the energy capture of the oscillating water column system. Based on the oscillating water column principle, Henriques et al. designed a self-powered ocean buoy, mainly used for long-term monitoring in remote areas (Henriques et al., 2016). The dimensions of the turbine and generator were optimized, and the evaluation results confirmed that the sea buoy has the characteristics of long-term deployment and less maintenance. Deng et al. designed an easy-to-install nearshore oscillating water column system with a surge front wall to improve conversion efficiency (Deng et al., 2020). The influence of front wall size on the hydrodynamic performance and conversion efficiency of the device is studied. Numerical results show that the freely surging front wall can significantly improve the performance of the device. Wang et al. considered the artificial viscous terms and used a fully nonlinear numerical model to simulate the dynamics of the oscillating water column system (Wang and Ning, 2020). The experimental results show that with the increase of air pressure, the influence of viscosity on wave force increases with the decrease of opening ratio. The oscillating water column system has lower construction costs and higher reliability. However, the high-efficiency frequency bandwidth of this wave energy conversion system is relatively narrow.

The overtopping system makes the waves enter the reservoir above sea level along the slope. Then, the seawater is released to drive the water turbine installed in the pipeline, thereby converting the wave energy into electricity. Liu et al. designed a novel circular ramp overtopping system (Liu et al., 2017). Then, laboratory experiments were conducted to study the influence of wave crest freeboard, ramp slope, and guide vane, which laid a solid foundation for future design work. Oliveira et al. analyzed the influence of the wave focusing wall on the overtopping system (Oliveira et al., 2016). The results show that the benefit of the use of wave focusing wall is affected by the wave height and the wave crest period, and the annual power generation is approximately doubled. Martins et al. studied the impact of ramp slope ( $\beta$ ) and the distance between the bottom of the reservoir and the device ( $S$ ) on the available power ( $P_d$ ) of the overtopping system at a practical scale (Martins et al., 2018). The results show that the optimal effective power can be achieved when  $S$  is constant and  $\beta$  is minimum. Aiming at the sea area with small waves and a large tidal range, Han et al. designed a multi-level reservoir system combined with inclined breakwater (Han et al., 2018). The results showed that the smaller the opening width, the larger the height ratio, and the 30° inclination angle could improve the system's power. Based on the results of conventional wave experiments, Buccino et al. deduced several design equations, which guided the design of the wave slot-cone generator (Buccino et al., 2015). The overtopping system can convert discontinuous and unstable wave energy into relatively stable water potential energy. However, the overtopping system is less efficient in sea areas with smaller wave heights.

The oscillating body system drives the internal mechanical transmission device through the up and down oscillation of the floating body, thereby converting wave energy into mechanical energy. Then, the generator converts the mechanical energy from the mechanical transmission device into electrical energy. Zhang et al. proposed an adaptive bistable mechanism composed of two symmetrical main springs and two auxiliary springs, which can solve the low energy absorption of traditional bistable wave energy devices under low amplitude excitation (Zhang et al., 2018). By adjusting the stiffness value of the spring, the adaptive bistable wave energy device can perform much better in low amplitude waves than the linear bistable device. Joe et al. proposed a novel wave turbine system with low deployment and maintenance costs consisting of a submerged body and a floating body (Joe et al., 2017). The sea experiment shows that the average power was 1.61W, the maximum power was 37.68W, and the average speed was 11.20 rpm under medium sea conditions, verifying the system's feasibility. Kim et al. conducted numerical and experimental studies on the performance of a point-absorber wave energy converter with a hydraulic power take-off system (Kim et al., 2019). According to the numerical model, the displacement and power of the hemispherical buoy were calculated to determine the best conditions corresponding to the maximum conversion power. Chen et al. studied the force and conversion efficiency of cylindrical and hemispherical buoys in the sea with low wave energy density (Chen et al., 2019). The experimental results show that the cylindrical buoy has the same response as the hemispherical buoy, but the force of the former was 194–1455% greater than that of the latter with the same diameter. Rodriguez et al. discussed the advantages and disadvantages of various power evaluation methods of the wave energy converter, suitable for the initial/mid-stage development of wave energy converters (Rodríguez et al., 2018). The analysis showed that the hybrid method among the listed power evaluation methods seems to be a more efficient and reliable method for evaluating the efficiency of wave energy converters. Oscillating body system has the advantages of low cost, high conversion efficiency, and high energy capture width ratio, which is the main form of using wave energy at present.

Although considerable progress has been made in the development and utilization of wave energy in recent years, further research on the application of wave power technology to small unmanned marine vehicles such as AUVs is needed. Furthermore, most previous research did not have practical demonstrations and mainly focused on numerical simulation. In order to solve the above problems, this article designs an extended-range wave-powered autonomous underwater vehicle (WPAUV) without changing the streamlined body for underwater wireless sensor networks, which are propelled by wave energy. The extended-range WPAUV converts the wave energy in the working environment into electric energy to expand the cruising mileage. A physical prototype of an extended-range WPAUV was manufactured, and laboratory tests and field tests were conducted to evaluate the power generation performance of the system. Compared with other environmental energy harvesting methods, this extended-range WPAUV has the advantages of higher efficiency and negligible changes in the original shape. The extended-range WPAUV converts irregular wave energy into electrical energy through an oscillating floater, extending autonomous mission duration and powering internal sensors. With the massive application of distributed underwater

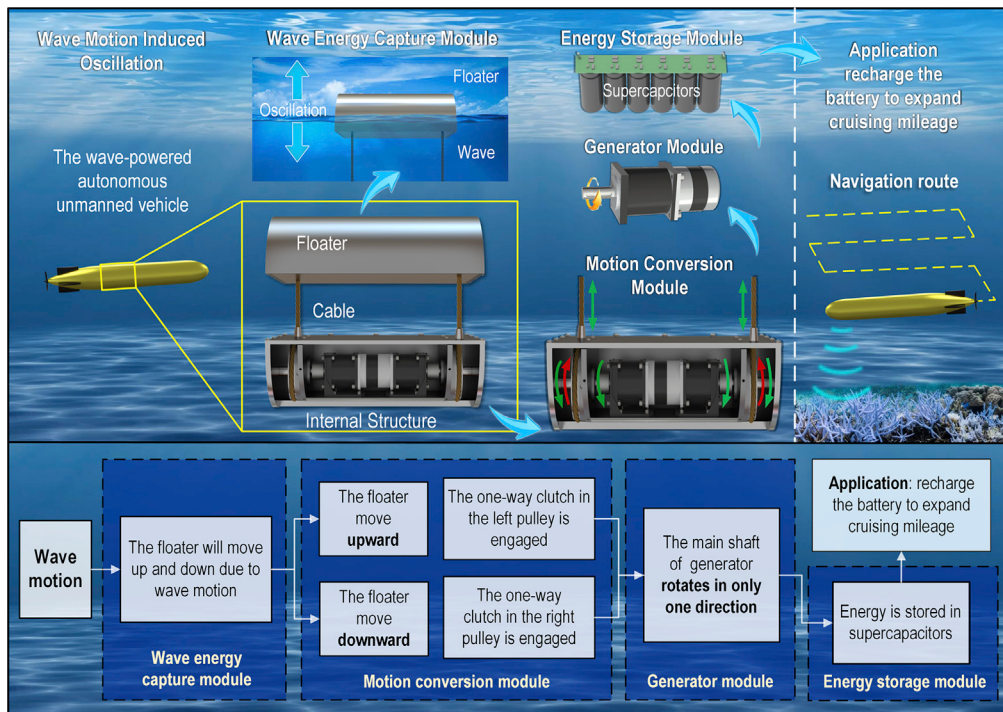


**Figure 1.** Flow chart of the proposed extended-range wave-powered autonomous underwater vehicle

sensing devices such as AUVs, ocean-bottom seismometers, and smart buoys, the concept of underwater wireless sensor network is proposed. Various nodes in the underwater wireless sensor network can support persistent ocean sensing by harvesting environment energy.

## RESULTS AND DISCUSSION

### System design

The general architecture of the extended-range WPAUV is based on the cable-pulley mechanism for applying in underwater wireless sensor networks, as shown in Figure 1. The proposed system consists of four main modules: (1) wave energy capture module, (2) motion conversion module, (3) generator module, and (4) electric energy storage module. As shown in the left area of Figure 1, the wave energy capture module is a semi-cylindrical floater connected to the main body of the extended-range WPAUV through two cables, which can move up and down with the ocean waves. The motion conversion module mainly contains cable-pulley mechanisms, which can convert the up and down movement of the floater into a one-way rotation of the generator. Therefore, the wave energy is converted into electrical energy through a generator module driven by unidirectional rotation, significantly improving reliability and power generation efficiency. The electric energy storage module is designed to store the electrical energy in the supercapacitor, which is applied to charging the battery to expand the cruising mileage of extended-range WPAUV, as described in the right part of Figure 1.

The wave energy capture module comprises a semi-cylindrical floater, two cables, and two waterproof sealing rings. One end of the cable is connected to the bottom of the semi-cylindrical floater, and the other end is wrapped around a pulley inside an extended-range WPAUV. When the extended-range WPAUV runs out of electricity, the semi-cylindrical floater will be released. When the wave passes through the bottom of the floater, the floater will move upward owing to the vertical component of the wave motion. After the wave passes the floater, the floater moves downward. Therefore, the floater can oscillate continuously at sea level under the action of waves. When the battery of the extended-range WPAUV is fully charged, the floater is retracted, so that the streamlined body is not changed. Therefore, the motion performance of the extended-range WPAUV will not be affected. The working principle of the extended-range WPAUV is shown in Figure 2.

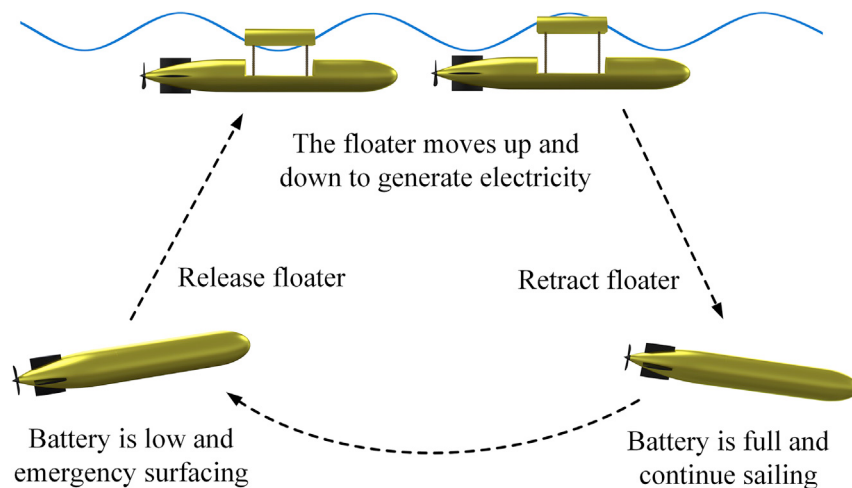


**Figure 2.** The work principle sketch map of the extended-range wave-powered autonomous underwater vehicle

The motion conversion module is the core module of the extended-range WPAUV, converting the up-and-down oscillation into unidirectional rotational motion. The motion conversion module mainly contains a cable-pulley mechanism, as indicated in Figure 3. As shown in Figure 4, a pulley wrapped with a cable is installed on the transmission shaft through a one-way clutch. The outer ring of the one-way clutch is fixed to the pulley by a flat key, and the inner ring is fixed to the transmission shaft by a flat key. The two ends of the transmission shaft are installed between the side plate and the middle plate through two deep groove ball bearings. An inner ring, an outer ring, and a coil spring are provided between the pulley and the middle plate. One end of the coil spring is fixed on the inner ring, and the other is fixed on the outer ring. The inner ring is welded to the right side of the pulley, and the outer ring is welded to the left side of the middle plate. The velocity of the cable and the angular velocity of the pulley has the following relationship:

$$\dot{S} = \omega \cdot R \quad (\text{Equation 1})$$

where  $\dot{S}$ ,  $\omega$ ,  $R$  represent the velocity of the cable, the angular velocity of the pulley, and the radius of the pulley, respectively. The pulley transmits the rotary motion to the generator shaft through the main shaft and the gearbox according to the following relationship:

$$\omega = i \cdot \omega_g \quad (\text{Equation 2})$$

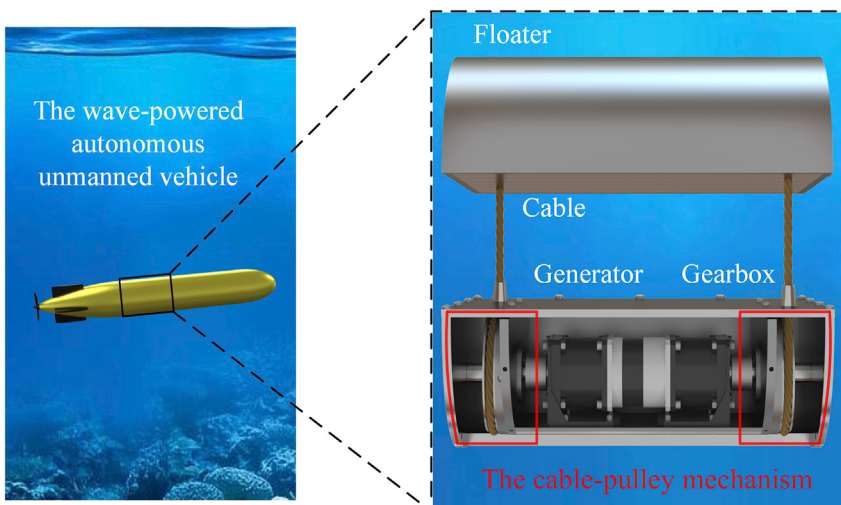


**Figure 3.** The cable-pulley mechanism of the motion conversion module

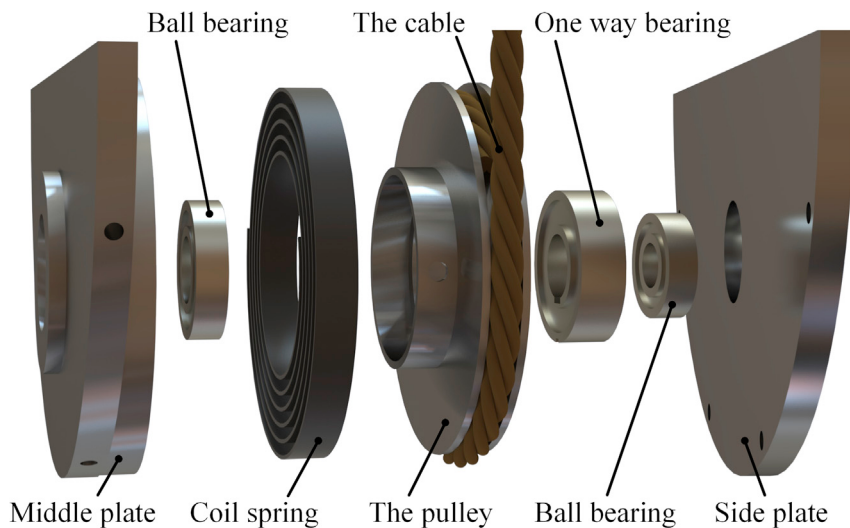


**Figure 4. The exploded diagram of the cable-pulley mechanism**

where  $i$  signifies the transmission ratio of the planetary gearbox and  $\omega_g$  represents the rotation speed of the generator shaft. From Equations 1 and 2 the relationship between the linear movement of the cable and the rotational movement of the pulley can be known.

When the wave passes the floater, the floater drives the two cables to move upward. At this time, the left pulley rotates clockwise, and the right pulley rotates counterclockwise. The one-way clutch in the right pulley is disengaged, and the one-way clutch in the left pulley is in an engaged state and transmits torque. Then the transmission shaft rotates clockwise, and the generator shaft rotates clockwise through the coupling, as shown in Figure 5A. After the wave passes the floater, the left pulley rotates counterclockwise, and the right pulley rotates clockwise under the action of the two cable-pulley mechanisms. The one-way clutch in the left pulley is disengaged, and the one-way clutch in the right pulley is in an engaged state and transmits torque. Then the transmission shaft rotates clockwise, and the generator shaft rotates clockwise through the coupling, as shown in Figure 5B. In this way, the up and down oscillation of the floater is converted into a unidirectional rotation of the generator shaft.

As shown in Figure 6, the generator module includes a dual-axis generator and two planetary gearboxes connected to the shell of the extended-range WPAUV through screws. Owing to the small internal space of the extended-range WPAUV, DC brushless motors (model 57BL55S06-230TF9) are selected. The motor has a small volume and weight, and the rotor inertia and copper losses are also small. The two planetary gearboxes are connected with a dual-shaft generator, whose function is to increase the rotation speed and enhance the power generation performance. The shafts of the two planetary gearboxes are, respectively,

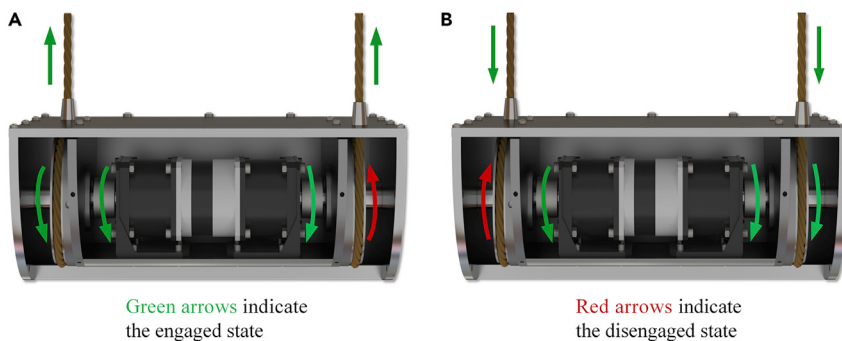


**Figure 5. Working state of the motion conversion module**

- (A) Operating state 1.
- (B) Operating state 2.

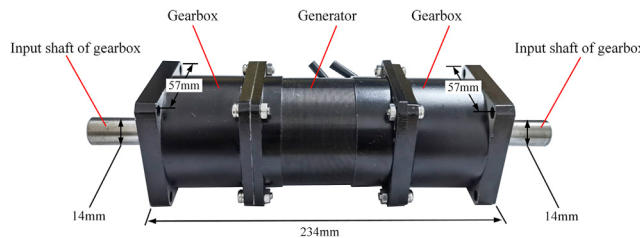


**Figure 6.** Brushless DC motor with two planetary gearboxes

connected with the transmission shaft through a coupling. The parameters of the generator and planetary gearbox are shown in [Table 1](#).

The oscillating motion of the wave is transmitted to the generator through the wave energy capture module and the motion conversion module. The generation of waves is affected by multiple factors, such as wind, gravity, and air pressure. Therefore, the actual waves are irregular. The amplitude and frequency of the waves are constantly changing, which causes the current generated by the generator to be unstable. After rectifying the current and regulating the voltage, the current is suitable for electrical loads and charging the battery. Supercapacitors have a fast response speed and long cycle life. The supercapacitor and rechargeable battery are connected in parallel to form a hybrid energy storage system, significantly improving the endurance performance of extended-range WPAUVs. As shown in [Figure 7](#), a charging circuit is designed to make the current stable and suitable for storage and charging. The charging circuit includes a rectifier circuit, a voltage regulator, a charging capacitor, and a load. The rectifier circuit is a three-phase full-wave rectifier circuit that can convert three-phase alternating current into pulse current. The voltage regulator is a three-pin adjustable positive voltage regulator belonging to the LM1117 series. Large capacity capacitors should be selected in the charging process to make the damping response characteristics more stable, as shown in [Figure 8](#).

### Modeling and analysis

This section establishes the system model. The system simulation is performed in order to investigate the factors affecting the system conversion efficiency and guide the prototype manufacturing. In addition, dynamic analysis of the system is performed. And system simulation of the extended-range WPAUV under different excitations is conducted utilizing dynamic simulation software MATLAB Simulink.

When the battery needs to be recharged, the extended-range WPAUV will be deployed at a position deep enough from the floater on the water surface. As wave motions mostly occur on the water surface, the main body of the extended-range WPAUV will be relatively fixed. The floater on the water surface will drive the motion conversion module with the fluctuation of the waves, which converts the wave energy into mechanical energy and drives the generator to generate electricity. In order to simplify the analysis, the oscillating motion of the floater on the water surface under the excitation of wave pressure is regarded as the simple harmonic motion near the equilibrium position. Therefore, the float device can be regarded as a mass-spring-damping system, as shown in [Figure 9](#). As the buoyancy of the floater is almost equal to gravity in the up and down oscillating motion, the buoyancy and gravity can be ignored during the analysis. The excitation force of the simple harmonic motion of the float only contains the vertical component of the wave pressure.

**Table 1.** Parameters of the generator module

Value	Parameters
24V	Rated voltage
3.6A	Rated current
60W	Rated power
0.6 Nm	Rated torque
1000 rpm	Rated speed
$4 \times 10^{-5} \text{ kg m}^2$	Rotor inertia
0.25Ω	Internal resistance
0.0403 V s/rad	Back electromotive voltage constant

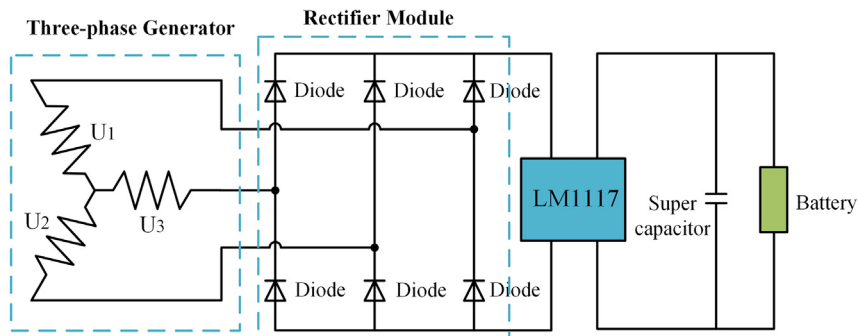


**Figure 7. Electric circuit of the electric energy storage module**

According to the Newton's second law, the motion equation of the floater is as follows:

$$m_F \ddot{z} = F_w + F_s + F_d \quad (\text{Equation 3})$$

where  $m_F$ ,  $\ddot{z}$ ,  $F_w$ ,  $F_s$ ,  $F_d$  represent the equivalent mass of the floater, acceleration of the vertical movement of the floater, the vertical component of the wave pressure, the elastic force of the compressed coil spring, and damping force of the system, respectively.

In order to determine  $F_w$ , the semi-cylindrical floater can be regarded as a cuboid floating on the sea surface with water depth of  $h$ , as shown in Figure 9. The length of the cuboid floater is  $l_a$ , the width is  $l_b$ , and the height is  $l_c$ . And  $l_d$  represents the draft depth of the floater. The incident wave with a wave height of  $H$  and a wavelength of  $\lambda$  propagates along the positive direction of the X axis. Therefore, the incident wave equation at time  $t$  is as follows:

$$\varphi(x, t) = \frac{H}{2} \cos(nx - \gamma t) \quad (\text{Equation 4})$$

where  $n$  represents the number of waves, and  $\gamma$  represents the frequency of the incident wave.

According to the Froude-Krylov assumption method, the vertical wave force acting on the floater can be expressed as:

$$F_w = C_z l_b \frac{\rho g H}{n} \cdot \frac{\cosh n(h - l_d)}{\cosh(nh)} \cdot \sin \frac{n l_a}{2} \cdot \cos \gamma t \quad (\text{Equation 5})$$

where  $C_z$  represents the vertical diffraction coefficient, which is related to the size of the cuboid floater, relative water depth  $h/\lambda$ , and wave steepness  $H/\lambda$ , etc. There is no definite analytical formula for  $C_z$ , and

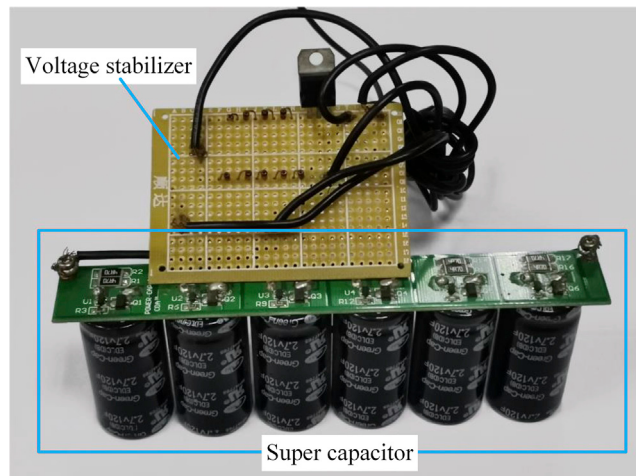


**Figure 8. Supercapacitor with the voltage stabilizer**

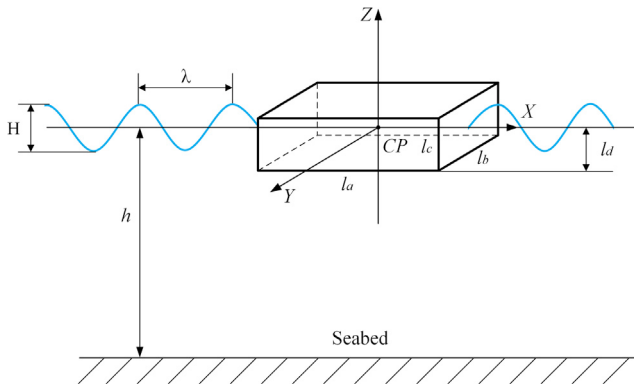


**Figure 9. The dynamic model of floater under wave excitation**

the exact value needs to be determined through experiment. Herbich J.B. recommends  $C_Z$  to be 2.7 based on the model test results (Boccotti, 2019).

Generally speaking,  $n$  and  $l_d$  are very small positive real numbers for the cuboid floater. Therefore,  $\frac{\cosh n(h-l_d)}{\cosh(nh)} \approx 1$ . Then the vertical wave force acting on the floater can be expressed as a cosine function that has the same frequency and phase as the wave motion at the origin of the coordinate:

$$F_w = F_0 \cos(\gamma t) \quad (\text{Equation 6})$$

where  $F_0$  is the amplitude of wave force, which is related to the shape and size of the floater, relative water depth  $h/\lambda$ , and wave steepness  $H/\lambda$ , etc. According to the Froude-Krylov assumption method, the approximate value of the vertical wave force acting on the floater is obtained. In the dry experiment, the landmark 370 servo-hydraulic test system is used to output this excitation force  $F_w$  to the prototype.

The dynamic analysis of the designed extended-range WPAUV is also carried out. As shown in Figure 10,  $F$  is defined as the excitation force and  $X$  is defined as the displacement. Using the Lagrangian formulation, the excitation force acting on the extended-range WPAUV can be written as:

$$\frac{d}{dt} \left( \frac{\partial T}{\partial \dot{X}} \right) - \frac{\partial T}{\partial X} + \frac{\partial E}{\partial X} + \frac{\partial D}{\partial X} = F \quad (\text{Equation 7})$$

where  $T$  represents the kinetic energy of the extended-range WPAUV,  $E$  represents the energy generated by the compressed coil spring, and  $D$  represents the energy generated by the damping effect.  $T$  can be given by the following equation:

$$T = 2 \times \left( \frac{1}{2} m_c \dot{X}^2 \right) + 2 \times \left( \frac{1}{2} J_p \omega^2 \right) + \frac{1}{2} J_b \omega^2 + \frac{1}{2} J_m \omega^2 + \frac{1}{2} J_{pg} \omega^2 + \frac{1}{2} J_g w_g^2 \quad (\text{Equation 8})$$

where  $m_c$  is the mass of the cable; and  $J_p$ ,  $J_b$ ,  $J_m$ ,  $J_{pg}$ ,  $J_g$  represent the inertia of the pulley, one-way bearing, main shaft, planetary gearbox, and generator, respectively. As the buoyancy of the floater is almost equal to gravity in the up and down oscillating motion, the buoyancy and gravity are ignored in the analysis process. Considering that  $\dot{X} = \dot{S}$ , and substituting Equations 1 and 2 into Equation 8, the equation can be simplified to

$$T = \frac{1}{2} \left( 2m_c + \frac{2J_p + J_b + J_m + J_{pg} + \frac{J_g}{R^2}}{R^2} \right) \dot{X}^2 \quad (\text{Equation 9})$$

The elastic potential energy  $E$  and the damping effect  $D$  can be written as:

$$E = \frac{1}{2} k_s \emptyset^2 \quad (\text{Equation 10})$$

$$D = \frac{1}{2} C_L \dot{X}^2 \quad (\text{Equation 11})$$

where  $k_s$  is the stiffness of the compressed coil spring,  $\emptyset$  is the deformation angle of the compressed coil spring,  $C_L$  represents the linear damping coefficient of the extended-range WPAUV.

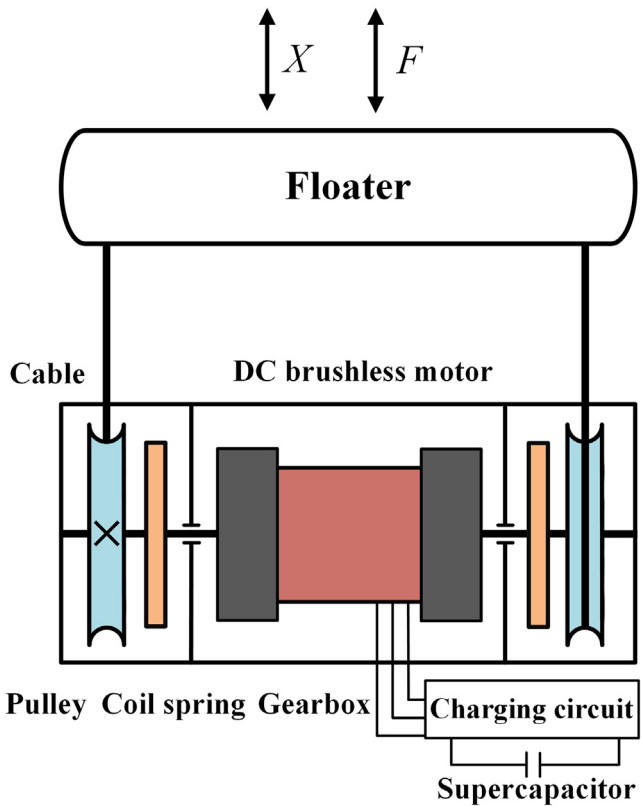


**Figure 10. The simplified dynamic model of the extended-range wave-powered autonomous underwater vehicle**

In addition, the input power can be expressed as the following equation:

$$P_{in} = C_L \dot{X}^2 \quad (\text{Equation 12})$$

The input power  $P_{in}$  is composed of  $P_f$  and  $P_E$ , where  $P_f$  represents the power loss owing to friction in the cable-pulley mechanism and the planetary gearbox, and  $P_E$  represents the generator power. Therefore, the input power  $P_{in}$  can also be written as:

$$P_{in} = P_f + P_E \quad (\text{Equation 13})$$

$$\eta_j \eta_{pg} \eta_g P_{in} = P_E \quad (\text{Equation 14})$$

where  $\eta_j$  represents the efficiency of the cable-pulley mechanism;  $\eta_{pg}$  represents the efficiency of the gearbox;  $\eta_g$  represents the efficiency of the generator. The following equation can be obtained by substituting Equation 12 into Equation 14:

$$\eta_j \eta_{pg} \eta_g C_L \dot{X}^2 = P_E \quad (\text{Equation 15})$$

A dual-axis brushless DC motor was selected as the generator. As described in the reference (Xie et al., 2020), the power of the generator can be expressed as:

$$P_E = C_R \omega_g^2 \quad (\text{Equation 16})$$

where  $C_R$  represents the rotational damping coefficient of the generator connected to the charging circuit.  $C_R$  can be expressed as:

$$C_R = \frac{1.5 K_e^2}{R_e + R_i} \quad (\text{Equation 17})$$

where  $K_e$  is the back electromotive force constant of the DC brushless motor,  $R_e$  is the external resistance of the charging circuit, and  $R_i$  is the internal resistance of the generator.

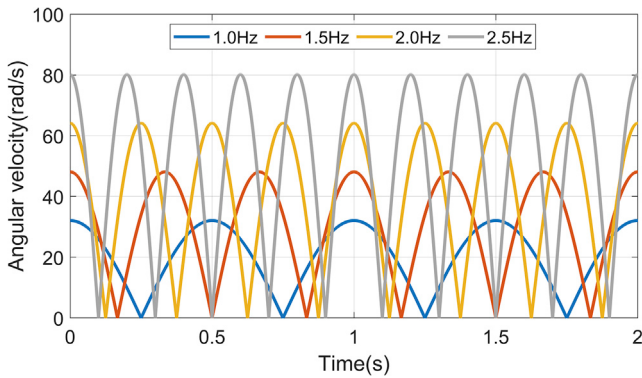


**Figure 11.** The angular velocity of the generator shaft for an amplitude of 12 mm at different frequencies

Considering that  $\dot{X} = \dot{S}$  and substituting Equations 1, 2, 16, and 17 into Equation 15, the following equation can be obtained:

$$C_L = \frac{1.5K_e^2}{\eta_j \eta_{pg} \eta_g (R_e + R_i) i^2 R^2} \quad (\text{Equation 18})$$

Substituting Equations 9–11 into Equation 7, the following equation can be obtained:

$$F = \left( 2m_c + \frac{2J_p + J_b + J_m + J_{pg} + \frac{J_g}{i^2}}{R^2} \right) \ddot{X} + \frac{k_s X}{R^2} + C_L \dot{X} \quad (\text{Equation 19})$$

Therefore, the equivalent mass of the entire system can be expressed as follows:

$$m_{eq} = 2m_c + \frac{2J_p + J_b + J_m + J_{pg} + \frac{J_g}{i^2}}{R^2} \quad (\text{Equation 20})$$

In the up and down oscillation movement, the float overcomes the elastic force of the compressed coil spring to move upward, and the elastic force of the compressed spring drives the float to move downward through the cables. Therefore, the upward and downward dynamic cycles can be described as:

$$F = \begin{cases} \left( 2m_c + \frac{2J_p + J_b + J_m + J_{pg} + \frac{J_g}{i^2}}{R^2} \right) \ddot{X} + \frac{k_s X}{R^2} + \left( \frac{1.5K_e^2}{\eta_j \eta_{pg} \eta_g (R_e + R_i) i^2 R^2} \right) \dot{X} & \text{upward progress} \\ \left( 2m_c + \frac{2J_p + J_b + J_m + J_{pg} + \frac{J_g}{i^2}}{R^2} \right) \ddot{X} - \frac{k_s X}{R^2} + \left( \frac{1.5K_e^2}{\eta_j \eta_{pg} \eta_g (R_e + R_i) i^2 R^2} \right) \dot{X} & \text{downward progress} \end{cases} \quad (\text{Equation 21})$$

The simulation software MATLAB is used to analyze the angular velocity of the generator shaft to obtain the kinetic relationship of the cable-pulley mechanism. The floater is excited by sinusoidal displacements of different frequencies with an amplitude of 12 mm. The angular velocity of the generator shaft is shown in Figure 11. Figure 11 reveals that the angular velocity of the generator shaft increases with the increase of the excitation frequency. Moreover, owing to the adoption of the cable-pulley mechanism, the main shaft of the generator can only rotate in one direction, which can improve the energy conversion efficiency.

In order to obtain the linear damping coefficient of the extended-range WPAUV, the parameters in Equation 18 can be estimated as follows: The efficiency of the cable-pulley mechanism  $\eta_j = 0.91$ , the efficiency of planetary gearbox  $\eta_{pg} = 0.97$ , the efficiency of the generator  $\eta_g = 0.97$ . In addition, other parameters used for calculation are listed in Table 2. Substituting these values into Equation 18, the linear damping

**Table 2. The parameters of the extended-range WPAUV**

Value	Parameters
2.212 kg	The mass of the cable $m_c$
$1.426 \times 10^{-4} \text{ kg m}^2$	Inertia of the pulley $J_p$
$1.438 \times 10^{-5} \text{ kg m}^2$	Inertia of one-way bearing $J_b$
$2.123 \times 10^{-3} \text{ kg m}^2$	Inertia of main shaft $J_m$
$1.5 \times 10^{-5} \text{ kg m}^2$	Inertia of planetary gearbox $J_{pg}$
$4 \times 10^{-5} \text{ kg m}^2$	Inertia of DC brushless motor $J_g$
2, 5, 10Ω	External resistance $R_e$
0.25Ω	Internal resistance $R_i$
1:15	Transmission ratio of gearbox $n$
0.0403V·s/rad	Back electromotive voltage constant $K_e$

coefficient can be calculated. [Figure 12](#) shows the linear damping coefficient under different external loads, where the best linear damping coefficient can be obtained by changing the external load. According to [Equation 18](#), the linear damping coefficient can also be adjusted to adapt to different ocean conditions by changing other parameters, such as the transmission ratio of the planetary gearbox. In addition, the simulation software MATLAB is used to investigate the force-displacement curves for different frequencies with an amplitude of 12mm and an external resistance of  $2\Omega$ , as shown in [Figure 13](#). The curve reflects that as the frequency increases, the average value of the input force gradually increases.

### Experiment details

The dry experiment was performed to further study the factors that affect the output power of the system and how these factors affect the output power. Then, all the data obtained in the dry experiment are analyzed to evaluate the energy conversion efficiency and reliability of the prototype. The dry experiment was carried out using a Landmark 370 servo-hydraulic test system from Mechanical Testing and Sensing (MTS) Systems Corporation, as shown in [Figure 14](#). [Figure 14A](#) represents a panoramic view of the Landmark 370 servo-hydraulic test system. The main technical parameters of the Landmark 370 servo-hydraulic test system are shown in [Table 3](#). As shown in [Figure 14B](#), a full-scale prototype of an extended-range WPAUV was manufactured two months ago. The upper and lower ends of the prototype are clamped by 647 hydraulic wedge grippers, respectively, as shown in [Figure 14C](#). The force-displacement signals are captured by the force sensor and displacement sensors integrated into the testing machine at a sampling frequency of 300 Hz and displayed on the computer monitor shown in [Figure 14D](#). As shown in [Figure 14E](#), three replaceable resistors are separately connected to the three-phase output of the generator as external loads. When the external load is 2, 5, and  $10\Omega$ , respectively, the prototype is excited by sinusoidal waves with different amplitudes from 6 mm to 12 mm and different frequencies of 1 Hz–3 Hz in order to verify its performance. The voltage signal of the single-phase external load is captured by the DS1102Z-E digital oscilloscope in [Figure 14F](#). Then, all the data obtained in the dry experiments are recorded, as shown in [Figure 14G](#).

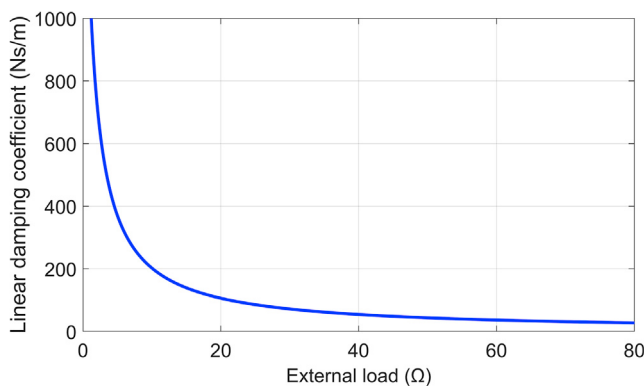


**Figure 12. The linear damping coefficient with different external loads**

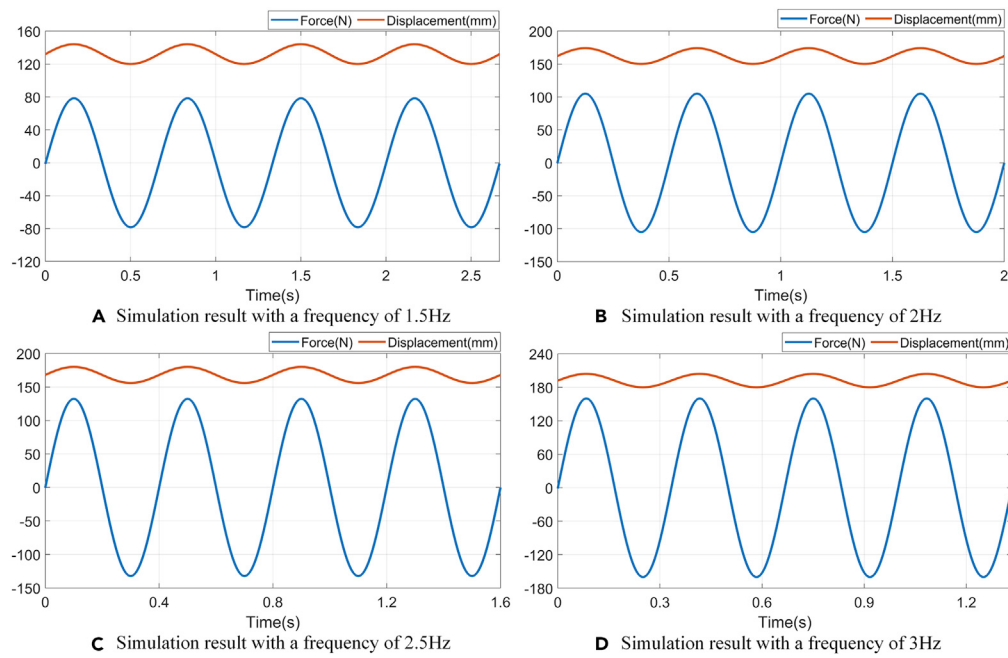


**Figure 13. The simulation results for frequencies of 1.5, 2, 2.5, and 3 Hz with an amplitude of 12 mm and an external resistance of  $2\Omega$**

- (A) Simulation result with a frequency of 1.5Hz.
- (B) Simulation result with a frequency of 2Hz.
- (C) Simulation result with a frequency of 2.5Hz.
- (D) Simulation result with a frequency of 3Hz.

In addition, in order to further verify the feasibility of the prototype, the field experiments, as shown in [Figure 15](#), were conducted under first-class sea conditions (the amplitude is 0 to 0.1m, the frequency is about 0.8Hz). [Figure 15A](#) shows the various experimental equipment required for the field experiment. As shown in [Figure 15B](#), the three-phase output of the generator is, respectively, connected to three external resistors of  $2\Omega$ . [Figure 15C](#) shows a prototype of the extended-range WPAUV assembled one month ago. The uninterruptible power supply system demonstrated in [Figure 15D](#) provides the required 220V power supply for the field experiment. The wave maker in [Figure 15E](#) can generate harmonic waves of different amplitudes at the set frequency through the control box. The control mode of the wave maker selects the intermittent mode, which can avoid the influence of multiple reflections of waves on the experimental results. At the same time, the rear end of the wave maker is close to the pool wall. From the top view, the outlet direction of the wave maker is perpendicular to the pool wall, which can avoid ripple interference caused by the pool wall as much as possible. The wave frequency generated by the wave maker is 0.8, 1.0, 1.2, and 1.4Hz, and the wave amplitude is 20, 30, 40, and 50mm, respectively. The wave amplitude is measured by a wave height gauge connected to a laptop, as shown in [Figure 15E](#). The prototype of the extended-range WPAUV is placed at a distance of 1.2m from the wave maker to avoid the influence of turbulence at the exit of the wave maker. The bottom of the prototype is anchored to the bottom of the pool. The voltage waveform of a single external resistor is recorded by a DS1102Z-E digital oscilloscope. In order to further verify that the captured wave energy can be effectively utilized by extended-range WPAUV, the supercapacitor charge and discharge experiment were performed.

### Output characterization of the system

This section mainly analyzes the output characterization of the system through dry experiments, field experiments, and supercapacitor charge-discharge experiments. Mechanical efficiency is an important indicator to evaluate the performance of the prototype under different experimental conditions. In order to evaluate the performance of the prototype, the mechanical efficiency can be expressed as:

$$\eta_M = \frac{\eta_{AUV}}{\eta_E} \quad (\text{Equation 22})$$

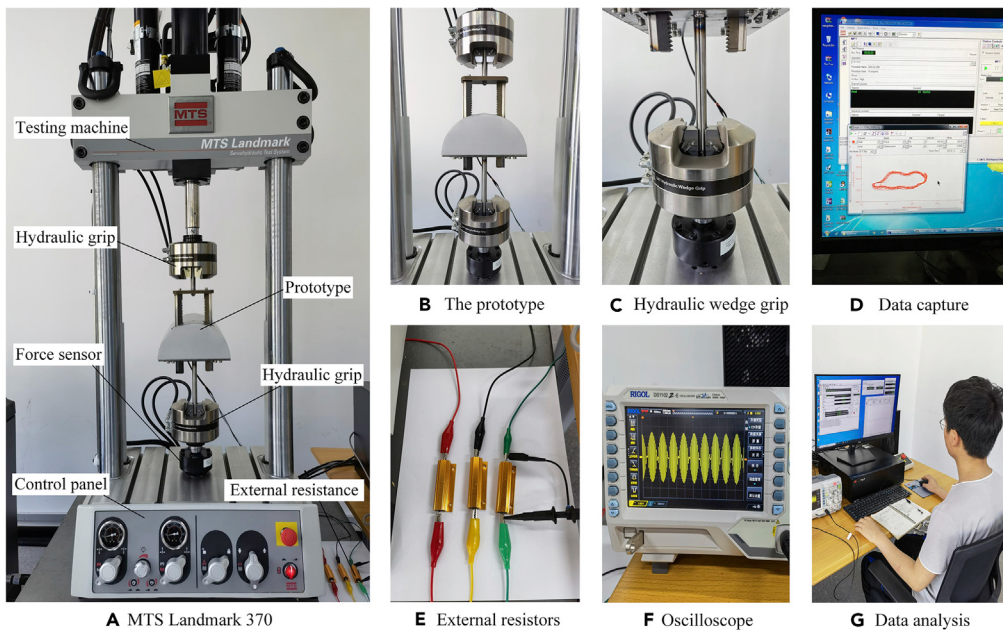


**Figure 14. The dry experiment of the prototype in the laboratory**

(A) MTS Landmark 370.

(B) The prototype.

(C) Hydraulic wedge grip.

(D) Data capture.

(E) External resistors.

(F) Oscilloscope.

(G) Data analysis.

where  $\eta_E$  represents the electrical efficiency of the prototype, which can be calculated by the following formula:

$$\eta_E = \frac{R_e}{R_e + R_i} \quad (\text{Equation 23})$$

Moreover,  $\eta_{AUV}$  represents the total efficiency of the prototype, which can be written as follows:

$$\eta_{AUV} = \frac{P_{out(ave)}}{P_{in(ave)}} \quad (\text{Equation 24})$$

where  $P_{out(ave)}$  expresses the average output electric power.  $P_{in(ave)}$  signifies the average input mechanical power in one cycle, which can be obtained as follows:

$$P_{in(ave)} = \frac{\Delta W}{T} \quad (\text{Equation 25})$$

where the input mechanical power  $\Delta W$  in one cycle can be obtained by calculating the area enclosed by each force-displacement loop.  $T$  indicates a cycle of sinusoidal excitation.

**Table 3. Main technical parameters of the Landmark 370 servo-hydraulic test system**

Parameters	Valve	Unit	Accuracy
Actuator dynamic stroke	150	mm	1μm
Actuator total stroke	165	mm	1μm
Actuator force capacity	25	kN	–
Peak operation speed	3	m/s	–
Actuator rated flow	57	lpm	–

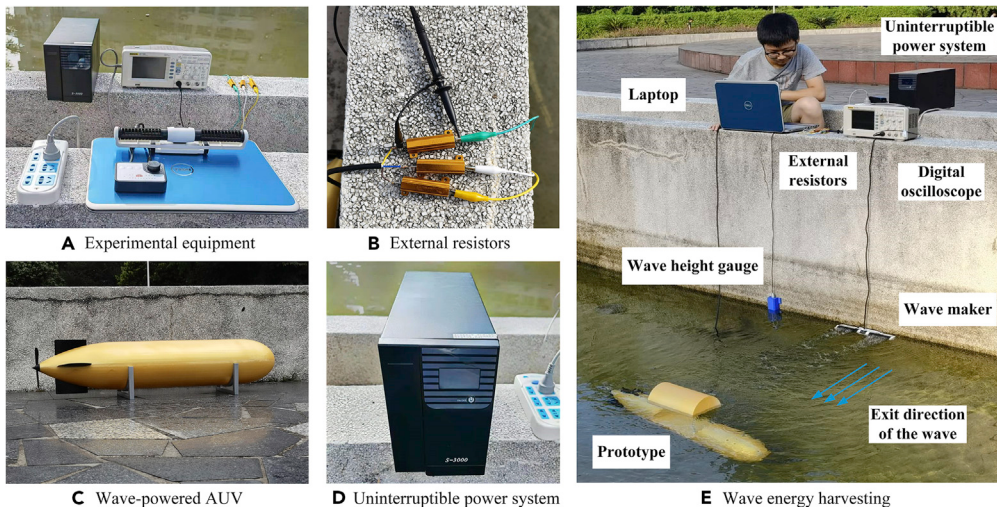


**Figure 15. Field experiment of the prototype and experimental configuration**

- (A) Experimental equipment.
- (B) External resistors.
- (C) Wave-powered AUV.
- (D) Uninterruptible power system.
- (E) Wave energy harvesting.

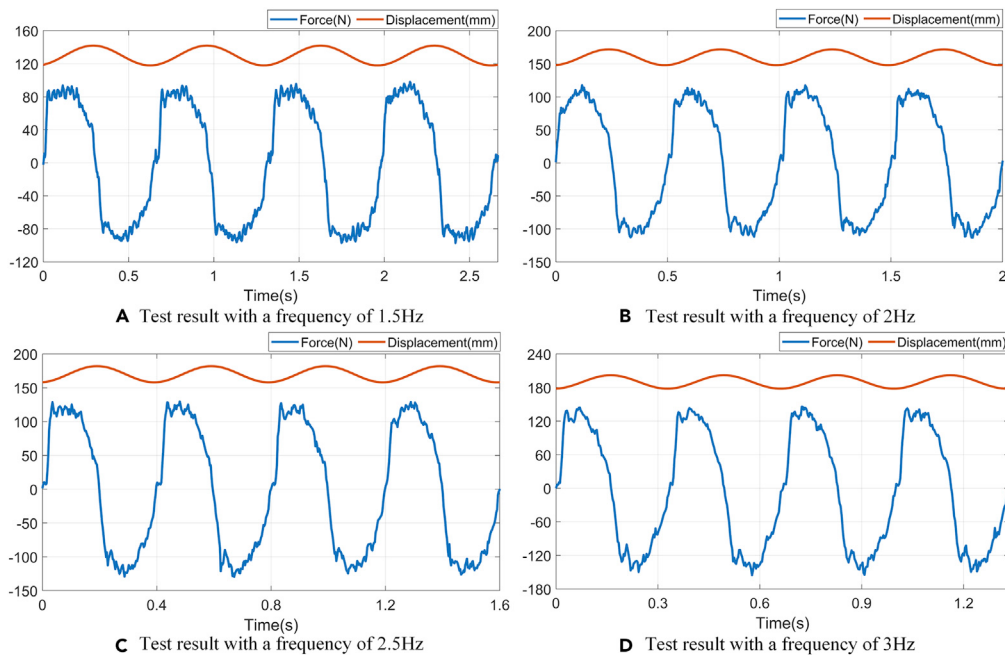
Figure 16 displays the force-displacement curves based on the dry experiments with an amplitude of 12mm and an external resistance of  $2\ \Omega$  at different frequencies. Figure 16 reveals that the input force curves of the dry experiments have some fluctuations compared with the simulation results. These fluctuations are particularly evident at the peaks and troughs of the input force curves. The following reasons may cause this phenomenon. First, the clearances and friction between the mechanical transmission elements in the prototype can cause slight impact and vibration. Second, some overshoot and fluctuation of the test machine controller will also affect the input force, especially at the peaks and troughs of the curves where the direction of the force changes suddenly. However, the basic trend and characteristics of the force-displacement curves based on the dry experiment are consistent with the simulated curves. These experimental results confirm the dynamic model of the extended-range WPAUV.

Figure 17 shows force-displacement loops with different amplitudes and resistances at a frequency of 3 Hz. Figure 17A only shows the force-displacement loop with a frequency of 3Hz and an external resistance of  $2\Omega$ . The input mechanical power  $\Delta W$  in a cycle can be obtained by calculating the area enclosed by each loop. According to the above method, the input mechanical power in other cases with an external resistance of  $2\Omega$  is shown in Table 4. Figure 17A reveals that as the wave amplitude increases, the force also increases. Figure 17B demonstrates the force-displacement loops for a frequency of 3 Hz and an amplitude of 12 mm at different external resistances. Figure 17B reveals that the force is almost reduced to zero when the displacement reaches the minimum or maximum. Moreover, the smaller the external resistance, the greater the force, because the equivalent damping increases as the external load decreases. This can be explained by Equation 18.

Under different amplitudes, frequencies, and external loads, the instantaneous voltage of a single external resistance is recorded in the dry test. This article only demonstrates the absolute values of the instantaneous voltage under different amplitudes and external resistances at a frequency of 3Hz, as shown in Figure 18. Instantaneous voltages in other situations can also be obtained. Therefore, the average output electric power can be written as:

$$P_{out} = 3 \times \frac{\int_0^T P_{instant} dt}{T} \quad (\text{Equation 26})$$

where  $P_{instant}$  signifies the instantaneous electric power, which can be calculated from the recorded instantaneous voltage and the external load  $R_e$ :



**Figure 16. The input force-displacement curves based on the dry experiments for frequencies of 1.5, 2, 2.5, and 3 Hz with an amplitude of 12 mm and an external resistance of 2Ω**

- (A) Test result with a frequency of 1.5Hz.
- (B) Test result with a frequency of 2Hz.
- (C) Test result with a frequency of 2.5Hz.
- (D) Test result with a frequency of 3Hz.

$$P_{\text{instant}} = \frac{U^2}{R_e} \quad (\text{Equation 27})$$

Therefore, the output electric power at different wave amplitudes, different wave frequencies, and different external resistors can be calculated. Table 5 lists the output electric power with an external resistance of 2 Ω at different amplitudes and frequencies. Applying Equation 24 to Tables 4 and 5, the total power of extended-range WPAUV can be calculated. It can be seen from Figure 18 that under the same wave frequency and the same external resistance, the higher the wave amplitude, the larger and more stable the

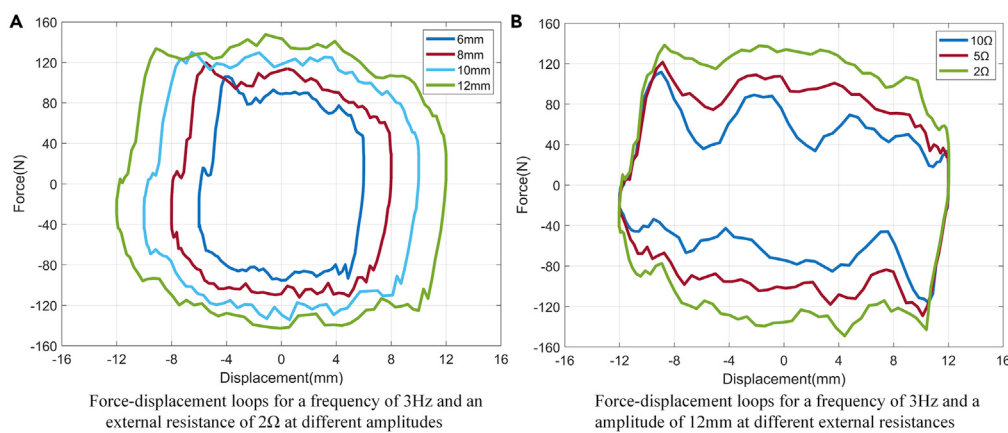


**Figure 17. The force-displacement loops with different amplitudes and different resistances at a frequency of 3 Hz**

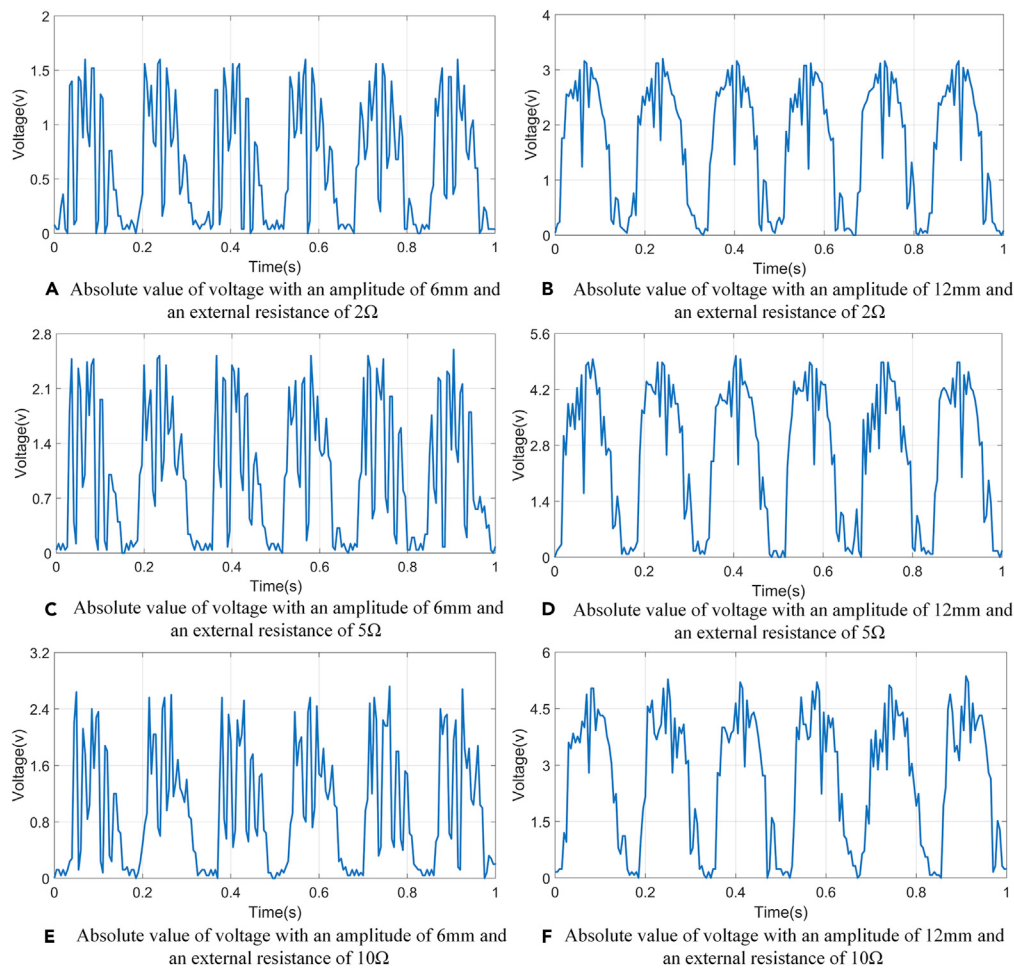
- (A) Force-displacement loops for a frequency of 3Hz and an external resistance of 2 Ω at different amplitudes.
- (B) Force-displacement loops for a frequency of 3Hz and an amplitude of 12 mm at different external resistances.

**Table 4. The input mechanical power with different amplitudes and frequencies at an external resistance  $2\Omega$** 

	1 Hz(W)	1.5 Hz(W)	2 Hz(W)	2.5 Hz(W)	3Hz(W)
6 mm	1.2349	2.0073	2.9976	4.2782	5.6186
8 mm	1.8080	3.1164	4.6526	6.5444	8.8737
10 mm	2.4686	4.2505	6.7500	9.1527	12.5868
12 mm	3.2026	5.6366	8.5954	12.3476	16.6956

instantaneous voltage of the external resistance. Under the same wave frequency and wave amplitude, the instantaneous voltage increases as the external resistance increases. However, as the resistance increases further, the increasing extent of the voltage gradually decreases.

Figure 19 reveals the mechanical efficiency of the prototype under different experimental conditions. As shown in Figure 19A, the mechanical efficiency is distributed between 20.41 and 81.56% for an external resistance of  $2\Omega$  at different frequencies and different amplitudes. The friction between motion components

**Figure 18. Absolute values of instantaneous voltage under different amplitudes and different external resistances at a frequency of 3Hz**

- (A) Absolute value of voltage with an amplitude of 6mm and an external resistance of  $2\Omega$ .
- (B) Absolute value of voltage with an amplitude of 12mm and an external resistance of  $2\Omega$ .
- (C) Absolute value of voltage with an amplitude of 6mm and an external resistance of  $5\Omega$ .
- (D) Absolute value of voltage with an amplitude of 12mm and an external resistance of  $5\Omega$ .
- (E) Absolute value of voltage with an amplitude of 6mm and an external resistance of  $10\Omega$ .
- (F) Absolute value of voltage with an amplitude of 12mm and an external resistance of  $10\Omega$ .

**Table 5. The output electrical power with different amplitudes and frequencies at an external resistance  $2\Omega$**

	1 Hz(W)	1.5 Hz(W)	2 Hz(W)	2.5 Hz(W)	3Hz(W)
6 mm	0.2244	0.5118	0.9319	1.5138	2.2800
8 mm	0.4081	0.9317	1.7457	2.8625	4.4976
10 mm	0.6390	1.4873	2.8459	4.8277	7.8761
12mm	0.9293	2.2243	4.3346	7.7167	12.1202

may explain the mechanical efficiency distributed between 20.41 and 81.56%. Therefore, the average mechanical efficiency, a more accurate indicator, is given to evaluate the performance of the system. According to the calculation, 45.35% is average mechanical efficiency. The mechanical efficiency increases with the increase of wave amplitude and wave frequency. As shown in Figure 19B, the mechanical efficiency is inversely proportional to the external resistance at an amplitude of 12mm and a frequency of 3Hz.

Figure 20 reveals the wave energy acquisition performance of the extended-range WPAUV. Figure 20A shows that the average output power is proportional to the wave amplitude and wave frequency, and inversely proportional to the external resistance. At 3Hz, increasing amplitude from 6mm to 12mm will increase average output power from 2.28W to 12.12W, which is 5 times the value of 3Hz and 6mm. When the amplitude is fixed at 12mm, increasing the frequency from 1Hz to 3Hz will increase the average output power from 0.93W to 12.12W, which is 13 times the value of 1Hz and 12mm. Overall, the influence of wave frequency on average output power is greater than that of wave amplitude. Figure 20B shows the time to charge the battery of the extended-range WPAUV under different experimental conditions. When the amplitude is 50mm, the frequency is 1.4Hz, and the external resistance is  $2\Omega$ , the charging time is the shortest, which is 2.65 days. The average charging time is 14.5 days under different experimental conditions. The fully charged battery can enable extended-range WPAUV to navigate 20 km at a time. The detailed parameters of the battery can be found in the reference (Phillips et al., 2009). The experimental results confirm the practicability of extended-range WPAUV.

In order to further verify that the extended-range WPAUV can effectively use the collected wave energy, supercapacitor charge and discharge experiments were carried out, as shown in Figure 21. Figure 21C shows the charging curves of different supercapacitors from 0.5F to 1.5F at a frequency of 0.8 Hz and an amplitude of 50 mm. A supercapacitor with the capacity of 1.5F can also be charged from 0V to 7V in the 110s, which manifests the practicability of the extended-range WPAUV. When the extended-range WPAUV needs to be charged, the wave energy is converted into electrical energy stored in the supercapacitors. Then, the supercapacitor will recharge the battery or power auxiliary devices of the extended-range WPAUV. Figure 21A shows that the supercapacitor can light up 43 parallel LED lights during the discharge

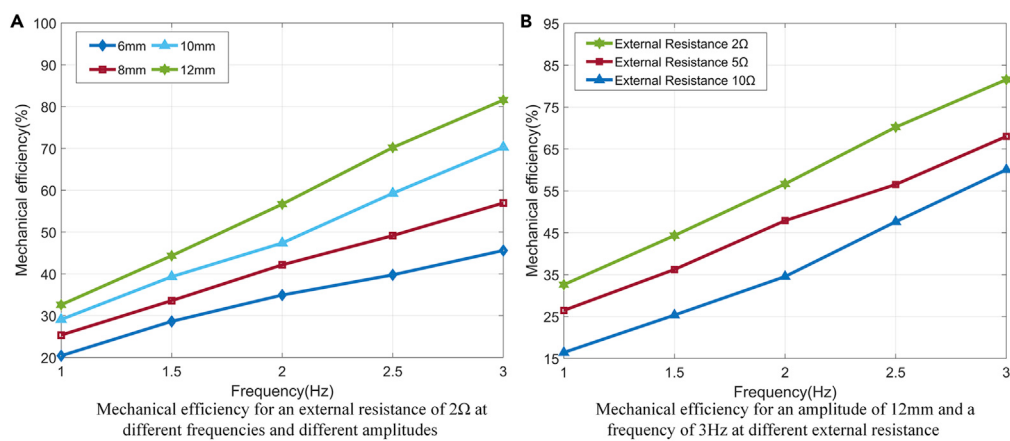


**Figure 19. The mechanical efficiency of extended-range wave-powered autonomous underwater vehicles for different external resistances, frequencies, and amplitudes**

(A) Mechanical efficiency for an external resistance of  $2\Omega$  at different frequencies and different amplitudes.

(B) Mechanical efficiency for an amplitude of 12mm and a frequency of 3 Hz at different external resistances.

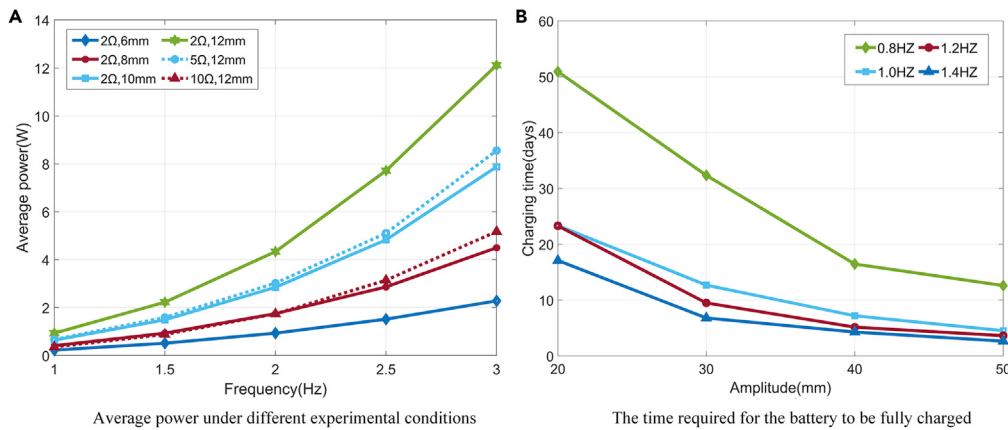


**Figure 20. Wave energy acquisition performance of the extended-range wave-powered autonomous underwater vehicles**

(A) Average power under different experimental conditions.

(B) The time required for the battery to be fully charged.

process. At the same time, as shown in Figure 21B, the propeller can also be driven. This high performance manifests that extended-range WPAUV can effectively harvest wave energy and convert it into electrical energy for powering external loads, including charging batteries.

In the field experiments, the wave maker can generate harmonic waves with amplitudes of 20, 30, 40, and 50 mm at frequencies of 0.8, 1.0, 1.2, and 1.4 Hz through the control box. The wave amplitude is measured by a wave height gauge connected to a data acquisition system, and an oscilloscope records the instantaneous voltage of a single external resistance. The instantaneous voltage increases slowly with the wave amplitude and wave frequency, as shown on the left side of Figure 22. The maximum instantaneous voltage can be close to 6.7V. Meanwhile, the instantaneous power and average power of the three external resistors are illustrated on the right side of Figure 22. As the wave frequency and wave amplitude increase, the instantaneous power and average power also increase slowly. At 50 mm amplitude and 1.4 Hz frequency, the maximum instantaneous power is 67.74W with an average of 10.18W. From Figure 22, the prototype can continuously generate a maximum of voltage and power from wave motion, even under the calm ocean conditions selected in the field experiments. Compared with the results of the dry experiment, the amplitude of the excitation wave in the field experiments is relatively larger. However, the wave energy capture ratio is lower than the former because the frequency of excitation waves in the field experiments is lower

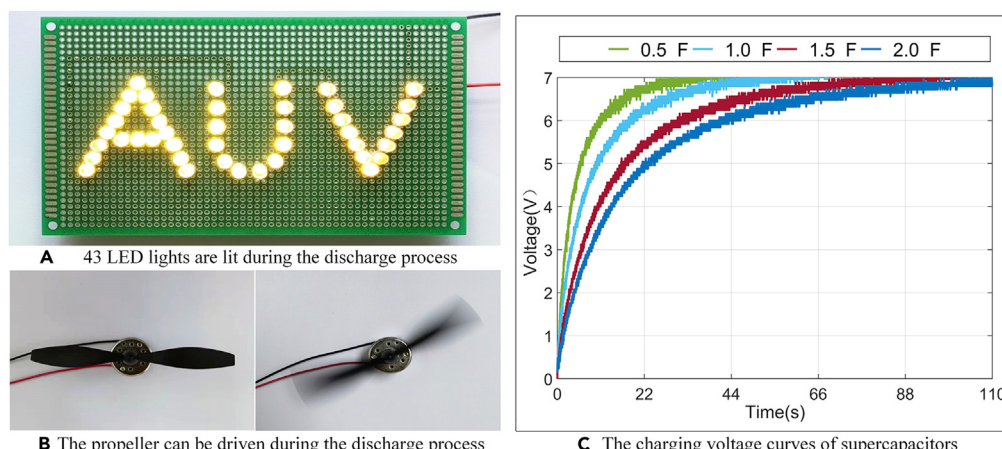


**Figure 21. The supercapacitor charge and discharge experiment**

(A) 43 LED lights are lit during the discharge process.

(B) The propeller can be driven during the discharge process.

(C) The charging voltage curves of supercapacitors.

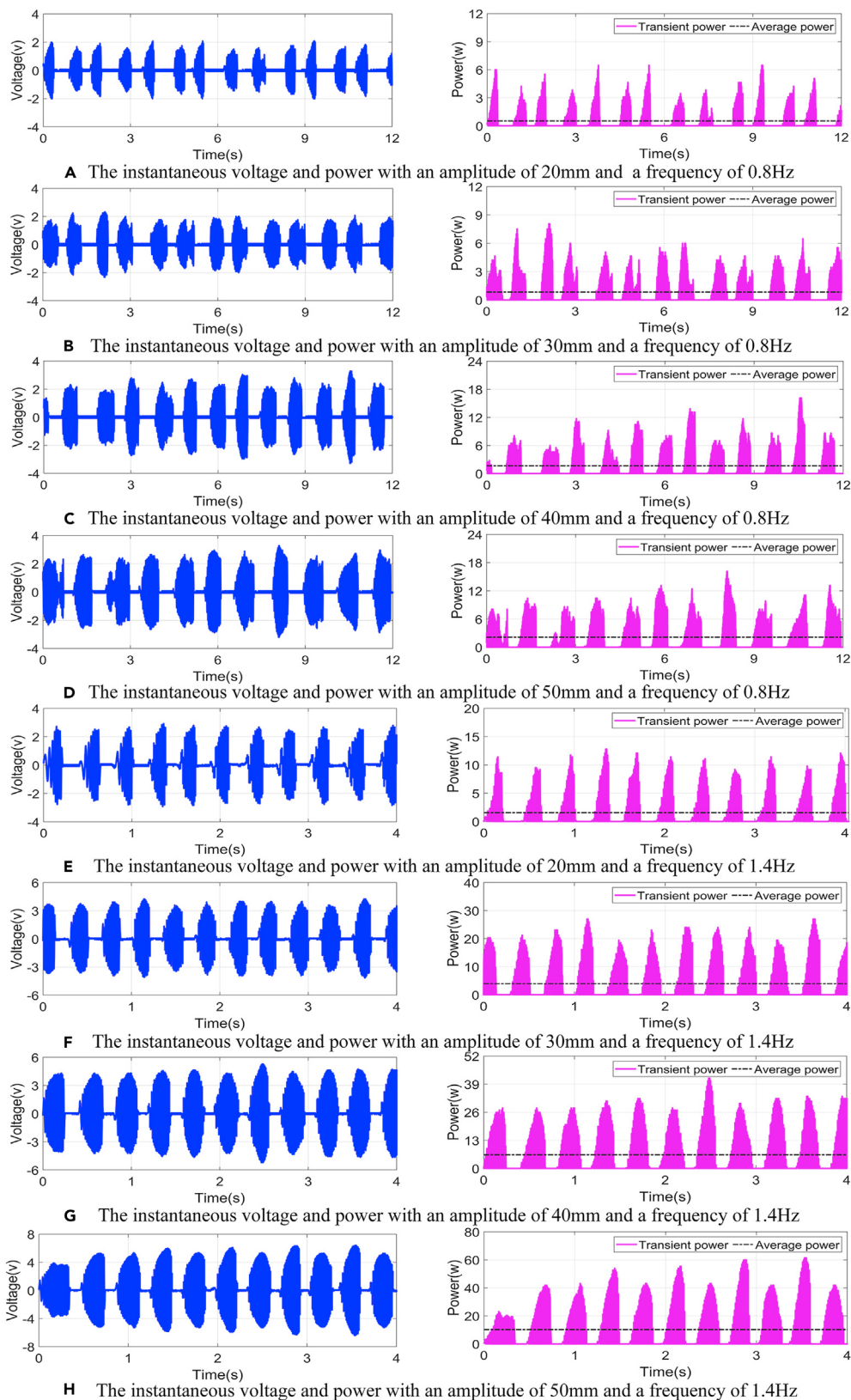


**Figure 22. The instantaneous voltage and instantaneous power of the field experiment at an external resistance of  $2\Omega$** 

- (A) The instantaneous voltage and power with an amplitude of 20mm and a frequency of 0.8Hz.
- (B) The instantaneous voltage and power with an amplitude of 30mm and a frequency of 0.8Hz.
- (C) The instantaneous voltage and power with an amplitude of 40mm and a frequency of 0.8Hz.
- (D) The instantaneous voltage and power with an amplitude of 50mm and a frequency of 0.8Hz.
- (E) The instantaneous voltage and power with an amplitude of 20mm and a frequency of 1.4Hz.
- (F) The instantaneous voltage and power with an amplitude of 30mm and a frequency of 1.4Hz.
- (G) The instantaneous voltage and power with an amplitude of 40mm and a frequency of 1.4Hz.
- (H) The instantaneous voltage and power with an amplitude of 50mm and a frequency of 1.4Hz.

than that in the dry experiments. In addition, the damping ratio of the prototype may not match the calm ocean conditions selected in the field experiment. The phase of the oscillating floater leads or lags the wave phase, which causes the wave to hinder the motion of the oscillating floater to a certain extent. Moreover, under the calm sea conditions, the time required for the battery to be fully charged is shown in [Figure 21B](#). [Table 6](#) shows the energy capture performance of various wave-powered unmanned marine vehicles with almost the same excitation parameters. Compared with other unmanned marine vehicles, the system proposed in this article is very encouraging.

Underwater wireless sensor networks are widely used in marine resources exploration, seabed search and rescue, underwater military reconnaissance, and marine environment monitoring. As shown in [Figure 23](#), the extended-range WPAUV is an essential node of underwater wireless sensor networks. The abbreviations in [Figure 23](#) are listed in [Table 7](#). The extended-range WPAUV usually works in deep-sea areas far from the coast where wave energy is enriched. Therefore, the extended-range WPAUV proposed in this article can capture abundant wave energy from the surrounding ocean environment. The collection of environmental energy has the advantages of simplicity, renewability, and cleanliness and dramatically expends the cruising mileage and working range of the WPAUV. When the battery of the extended-range WPAUV is fully charged, the semi-cylindrical floater is retracted, so that the streamlined fuselage is not changed and the resistance is reduced during navigation. The wave energy collected from the marine environment is mainly used to charge the battery to solve the disadvantage that the AUV needs to replace the battery frequently. The extended-range WPAUV regenerates 10.18W of energy at an amplitude of 50 mm and a frequency of 1.4 Hz, according to the results of the field test, and it takes 2.65 days to fully charge the battery of the extended range WPAUV. The fully charged battery can enable extended-range WPAUVs to navigate 20 km at a time. Therefore, the extended-range WPAUV proposed in this article can perform various tasks autonomously in a larger area. As shown in [Figure 23](#), in the future, this wave energy harvesting technology can be transplanted to other underwater wireless sensor network nodes, such as smart buoys and unmanned surface vessels, etc. The proposed WPAUV can realize the persistent power supply of various nodes to build the underwater wireless sensor network. The underwater wireless sensor network will allow uninterrupted large-area ocean data collection to become a reality.

### Conclusions and future work

This paper describes the design, modeling, simulation, and experimental study of the extended-range WPAUV based on a cable-pulley mechanism. Compared with other energy scavenging systems, this system has better performance under almost the same excitation parameters. Through theoretical analysis, simulation, and experiments, the power generation performance of the extended-range WPAUV was evaluated. Through theoretical analysis, it is concluded that the proposed system can scavenge wave energy effectively. The reliability and availability of the cable-pulley mechanism were demonstrated through simulation and dry experiments. Under different wave amplitudes and wave frequencies, the mechanical efficiency of

**Table 6. Comparison to other small unmanned marine vehicles**

No.	References	Energy Harvesting Technology	Excitation parameter		Regenerated average power (W)
			Frequency (Hz)	Amplitude (mm)	
1.	This work	Oscillation System	1.0	50	5.9
2.	Bracco et al. (2011)	Inertial System	1.0	100	2.2
3.	Bowker et al. (2015)	Flapping Foil System	0.8	80	1.0
4.	Townsend (2016)	Gyroscopic System	0.7	100	1.24

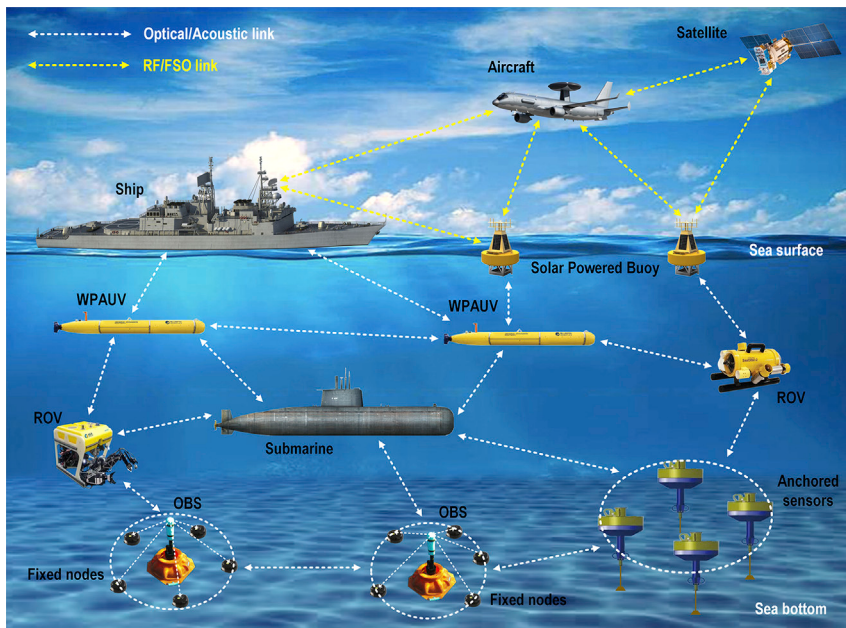


**Figure 23. Application of the extended-range wave-powered autonomous underwater vehicle in the underwater wireless sensor network**

extended-range WPAUV ranges from 20.41% to 81.56%. And 45.35% is the average mechanical efficiency. Under calm ocean conditions, the extreme instantaneous power measured in the field experiments was 67.74W, with an average of 10.18W. The time required for the battery of the extended-range WPAUV to be fully charged is 2.65 days, and the fully charged battery can enable the WPAUV to navigate 20 km at a time. This high-performance system enables WPAUV to be remotely recharged at sea, extending the mission period. In addition, this wave energy acquisition technology has a wide application prospect in the self-powered field of underwater wireless sensor network nodes such as smart buoys and unmanned surface vessels.

Currently, the proposed system still needs further field experiments and comprehensive performance optimization. The research work to be solved in the future is summarized as follows:

- (1) The ocean contains abundant energy including solar energy, wave energy, ocean current energy, ocean thermal energy, and so on. Therefore, it is also necessary to explore the potential of collecting other ocean energy (such as solar energy) as supplementary energy for AUVs.
- (2) The generation of waves is affected by multiple factors, such as wind, gravity, and air pressure, which cause the amplitude and frequency of waves to change constantly. However, the traditional rotating generator has poor adaptability to this special working condition. In future research, high-performance special generators should be developed for wave-powered AUVs.

**Table 7. Abbreviations in this paper**

Abbreviation	Full name
RF link	Radio frequency link
FSO link	Free space optics link
ROV	Remote operated vehicle
OBS	Ocean bottom seismometer
AUV	Autonomous underwater vehicle
WPAUV	Wave-powered autonomous underwater vehicle

- (3) Currently, the low energy conversion efficiency is one of the bottlenecks restricting the extensive use of wave power generation technology. Therefore, optimizing Maximum Power Point Tracking Control Methods of wave power generation technology is also a compelling issue to be solved.

### Limitations of the study

Through theoretical analysis, simulation, and experiments, the power generation performance of the extended-range WPAUV was evaluated. The results manifest that the extended-range WPAUV can effectively scavenge wave energy and convert it into electrical energy for expanding the cruising mileage. However, the simulation and experiments are performed under regular waves. In order to evaluate the performance of WPAUV more accurately, future research will be carried out under irregular waves in the near future.

### STAR★METHODS

Detailed methods are provided in the online version of this paper and include the following:

- KEY RESOURCES TABLE
- RESOURCE AVAILABILITY
  - Lead contact
  - Material availability
  - Data and code availability
- METHOD DETAILS
- QUANTIFICATION AND STATISTICAL ANALYSIS

### SUPPLEMENTAL INFORMATION

Supplemental information can be found online at <https://doi.org/10.1016/j.isci.2022.104738>.

### ACKNOWLEDGMENTS

This work was supported by the National Natural Science Foundation of China under Grants No. 51975490; and by the Science and Technology Projects of Sichuan under Grants Nos. 2021JDRC0096 and 2021JDRC0118; and by the Science and Technology Projects of Sichuan under Grants Nos. 2021YFSY0059 and 2020YFSY0070. Zutao Zhang and Yajia Pan are co-corresponding authors.

### AUTHOR CONTRIBUTIONS

H.L: Data curation, Writing-Original draft preparation, Software, Visualization; X.W: Visualization, Investigation; Z.Z: Conceptualization, Methodology, Supervision, Project administration, Resources; X.T: Formal analysis; Y.P: Supervision, Reviewing and Editing; C.D: Formal analysis; D.L: Software; A.A: Writing-Review & Editing; Y.X: Visualization.

### DECLARATION OF INTERESTS

The authors declare no competing interests.

Received: February 11, 2022

Revised: June 6, 2022

Accepted: July 7, 2022

Published: August 19, 2022

### REFERENCES

- Abido, M.Y., Mahmud, Z., Sánchez-Pérez, P.A., and Kurtz, S.R. (2022). Seasonal challenges for a California renewable-energy-driven grid. *iScience* 25, 103577. <https://doi.org/10.1016/j.isci.2021.103577>.
- Boccotti, P. (2019). Wave mechanics for ocean engineering. *J. Chem. Inf. Model.* 53, 1689–1699.
- Bowker, J.A., Townsend, N.C., Tan, M., and Shenoi, R.A. (2015). Experimental study of a wave energy scavenging system onboard autonomous surface vessels (ASVs). In MTS/IEEE Ocean. 2015–Genova Discov. Sustain. Ocean Energy a New World. <https://doi.org/10.1109/OCEANS-Genova.2015.7271484>.
- Bracco, G., Giorcelli, E., and Mattiuzzo, G. (2011). ISWEC: a gyroscopic mechanism for wave power exploitation. *Mech. Mach. Theory* 46, 1411–1424. <https://doi.org/10.1016/j.mechmachtheory.2011.05.012>.
- Buccino, M., Vicinanza, D., Salerno, D., Banfi, D., and Calabrese, M. (2015). Nature and magnitude of wave loadings at seawave slot-cane generators. *Ocean Eng.* 95, 34–58. <https://doi.org/10.1016/j.oceaneng.2014.11.038>.
- Chen, F., Duan, D., Han, Q., Yang, X., and Zhao, F. (2019). Study on force and wave energy conversion efficiency of buoys in low wave energy density seas. *Energy Convers. Manag.* 182, 182.

191–200. <https://doi.org/10.1016/j.enconman.2018.12.074>.

Chin, C.S., Jia, J., Hay King Chiew, J., Da Toh, W., Gao, Z., Zhang, C., and McCann, J. (2019). System design of underwater battery power system for marine and offshore industry. *J. Energy Storage* 21, 724–740. <https://doi.org/10.1016/j.est.2019.01.007>.

Deng, Z., Wang, L., Zhao, X., and Wang, P. (2020). Wave power extraction by a nearshore oscillating water column converter with a surging lip-wall. *Renew. Energy* 146, 662–674. <https://doi.org/10.1016/j.renene.2019.06.178>.

DeSantis, D., James, B.D., Houchins, C., Saur, G., and Lyubovsky, M. (2021). Cost of long-distance energy transmission by different carriers. *iScience* 24, 103495. <https://doi.org/10.1016/j.isci.2021.103495>.

Falcão Carneiro, J., and Gomes de Almeida, F. (2018). Model and simulation of the energy retrieved by thermoelectric generators in an underwater glider. *Energy Convers. Manag.* 163, 38–49. <https://doi.org/10.1016/j.enconman.2018.02.031>.

Falcão, A.F.d.O. (2010). Wave energy utilization: a review of the technologies. *Renew. Sustain. Energy Rev.* 14, 899–918. <https://doi.org/10.1016/j.rser.2009.11.003>.

Fenucci, D., Caffaz, A., Costanzi, R., Fontanesi, E., Manzari, V., Sani, L., Stifani, M., Tricarico, D., Turetta, A., and Caiti, A. (2016). WAVE: a wave energy recovery module for long endurance gliders and AUVs. In *Ocean. 2016 MTS/IEEE Monterey*. OCE 2016 1–5. <https://doi.org/10.1109/OCEANS.2016.7761136>.

Gøtske, E.K., and Victoria, M. (2021). Future operation of hydropower in Europe under high renewable penetration and climate change. *iScience* 24, 102999. <https://doi.org/10.1016/j.isci.2021.102999>.

Han, G., Kwon, Y.K., Kim, J.B., Lee, S., Bae, J., Cho, E.A., Lee, B.J., Cho, S., and Park, J. (2020). Development of a high-energy-density portable/mobile hydrogen energy storage system incorporating an electrolyzer, a metal hydride and a fuel cell. *Appl. Energy* 259, 114175. <https://doi.org/10.1016/j.apenergy.2019.114175>.

Han, Z., Liu, Z., and Shi, H. (2018). Numerical study on overtopping performance of a multi-level breakwater for wave energy conversion. *Ocean Eng.* 150, 94–101. <https://doi.org/10.1016/j.oceaneng.2017.12.058>.

Henriques, J.C.C., Portillo, J.C.C., Gato, L.M.C., Gomes, R.P.F., Ferreira, D.N., and Falcão, A.F.O.

(2016). Design of oscillating-water-column wave energy converters with an application to self-powered sensor buoys. *Energy* 112, 852–867. <https://doi.org/10.1016/j.energy.2016.06.054>.

Joe, H., Roh, H., Cho, H., and Yu, S.C. (2017). Development of a flap-type mooring-less wave energy harvesting system for sensor buoy. *Energy* 133, 851–863. <https://doi.org/10.1016/j.energy.2017.05.143>.

Khan, N., Kalair, A., Abas, N., and Haider, A. (2017). Review of ocean tidal, wave and thermal energy technologies. *Renew. Sustain. Energy Rev.* 72, 590–604. <https://doi.org/10.1016/j.rser.2017.01.079>.

Kim, S.J., Koo, W., and Shin, M.J. (2019). Numerical and experimental study on a hemispheric point-absorber-type wave energy converter with a hydraulic power take-off system. *Renew. Energy* 135, 1260–1269. <https://doi.org/10.1016/j.renene.2018.09.097>.

Liu, Z., Shi, H., Cui, Y., and Kim, K. (2017). Experimental study on overtopping performance of a circular ramp wave energy converter. *Renew. Energy* 104, 163–176. <https://doi.org/10.1016/j.renene.2016.12.040>.

López, I., Carballo, R., and Iglesias, G. (2020). Intra-annual variability in the performance of an oscillating water column wave energy converter. *Energy Convers. Manag.* 207, 112536. <https://doi.org/10.1016/j.enconman.2020.112536>.

Martins, J.C., Goulart, M.M., Gomes, M., das, N., Souza, J.A., Rocha, L.A.O., Isoldi, L.A., and dos Santos, E.D. (2018). Geometric evaluation of the main operational principle of an overtopping wave energy converter by means of Constructal Design. *Renew. Energy* 118, 727–741. <https://doi.org/10.1016/j.renene.2017.11.061>.

Niu, H., Ji, Z., Savvaris, A., and Tsourdos, A. (2020). Energy efficient path planning for Unmanned Surface Vehicle in spatially-temporally variant environment. *Ocean Eng.* 196, 106766. <https://doi.org/10.1016/j.oceaneng.2019.106766>.

Oliveira, P., Taveira-Pinto, F., Morais, T., and Rosa-Santos, P. (2016). Experimental evaluation of the effect of wave focusing walls on the performance of the Sea-wave Slot-cone Generator. *Energy Convers. Manag.* 110, 165–175. <https://doi.org/10.1016/j.enconman.2015.11.071>.

Phillips, A.B., Steenson, L., Harris, C., Rogers, E., Turnock, S.R., and Furlong, M. (2009). Delphin2 : An over actuated autonomous underwater vehicle for manoeuvring research (Part A-International Journal of Maritime Engineering).

<https://nora.nerc.ac.uk/id/eprint/507416/1/Delphin2.pdf>.

Rodríguez, C.A., Rosa-Santos, P., and Taveira-Pinto, F. (2018). Assessment of the power conversion of wave energy converters based on experimental tests. *Energy Convers. Manag.* 173, 692–703. <https://doi.org/10.1016/j.enconman.2018.08.009>.

Röhr, J.A., Lipton, J., Kong, J., Maclean, S.A., and Taylor, A.D. (2020). Efficiency limits of underwater solar cells. *Joule* 4, 840–849. <https://doi.org/10.1016/j.joule.2020.02.005>.

Townsend, N.C. (2016). Self-powered autonomous underwater vehicles: results from a gyroscopic energy scavenging prototype. *IET Renew. Power Gener.* 10, 1078–1086. <https://doi.org/10.1049/iet-rpg.2015.0210>.

Townsend, N.C., and Shenoi, R.A. (2016). Feasibility study of a new energy scavenging system for an autonomous underwater vehicle. *Auton. Robots* 40, 973–985. <https://doi.org/10.1007/s10514-015-9506-4>.

Wang, R. quan, and Ning, D. zhi (2020). Dynamic analysis of wave action on an OWC wave energy converter under the influence of viscosity. *Renew. Energy* 150, 578–588. <https://doi.org/10.1016/j.renene.2020.01.007>.

Xie, Q., Zhang, T., Pan, Y., Zhang, Z., Yuan, Y., and Liu, Y. (2020). A novel oscillating buoy wave energy harvester based on a spatial double X-shaped mechanism for self-powered sensors in sea-crossing bridges. *Energy Convers. Manag.* 204, 112286. <https://doi.org/10.1016/j.enconman.2019.112286>.

Xupeng, H., Wenbin, S., Hang, Z., Yanni, Z., Qiao, H., and Chaohui, W. (2020). Research of the hydrostatic transmission for deep-sea current energy converter. *Energy Convers. Manag.* 207, 112544. <https://doi.org/10.1016/j.enconman.2020.112544>.

Younesian, D., and Alam, M.R. (2017). Multi-stable mechanisms for high-efficiency and broadband ocean wave energy harvesting. *Appl. Energy* 197, 292–302. <https://doi.org/10.1016/j.apenergy.2017.04.019>.

Zhang, X., Tian, X., Xiao, L., Li, X., and Chen, L. (2018). Application of an adaptive bistable power capture mechanism to a point absorber wave energy converter. *Appl. Energy* 228, 450–467. <https://doi.org/10.1016/j.apenergy.2018.06.100>.

Zhou, Y., Zhang, C., and Ning, D. (2018). Hydrodynamic investigation of a concentric cylindrical OWC wave energy converter. *Energies* 11, 985. <https://doi.org/10.3390/en11040985>.

**STAR★METHODS****KEY RESOURCES TABLE**

REAGENT or RESOURCE	SOURCE	IDENTIFIER
<b>Software and algorithms</b>		
Microsoft Visio 2013	Microsoft	<a href="https://www.microsoft.com/zh-cn/microsoft-365/visio/flowchart-software">https://www.microsoft.com/zh-cn/microsoft-365/visio/flowchart-software</a>
MATLAB 2019a	Mathworks	<a href="https://www.mathworks.com/products/matlab.html">https://www.mathworks.com/products/matlab.html</a>
<b>Other</b>		
Landmark 370 servo-hydraulic test system	Mechanical Testing and Sensing (MTS) Systems Corporation	<a href="https://www.mts.com/en/products/materials/dynamic-materials-test-systems/landmark-servohydraulic">https://www.mts.com/en/products/materials/dynamic-materials-test-systems/landmark-servohydraulic</a>
DS1102Z-E digital oscilloscope	RIGOL	<a href="https://rigol.com">https://rigol.com</a>

**RESOURCE AVAILABILITY****Lead contact**

Further information and requests for resources and reagents should be directed to and will be fulfilled by the lead contact Zutao Zhang ([zzt@sjtu.edu.cn](mailto:zzt@sjtu.edu.cn)).

**Material availability**

This study did not generate new unique reagents.

**Data and code availability**

- All data reported in this paper will be shared by the [lead contact](#) upon reasonable request.
- This paper does not report original code.
- Any additional information required to reanalyze the data reported in this paper is available from the [lead contact](#) upon request.

**METHOD DETAILS**

All methods can be found in the main text. Please check the [System design](#) section for the design details of the system. Please check the [Modeling and analysis](#) section for the simulation and analysis details of the system. For details of the experimental design and equipment performance parameters, please refer to the [Experiment details](#) section.

Microsoft Visio 2013 is used to generate the visual images in the manuscript. MATLAB 2019a is used to process experimental data and generate visual images in the manuscript. A demo video is provided to introduce the whole article more vividly, as shown in [Video S1](#).

**QUANTIFICATION AND STATISTICAL ANALYSIS**

Microsoft Visio 2013 is used to generate the visual images in the manuscript. The voltage signals are captured by the DS1102Z-E digital oscilloscope. The force-displacement signals are captured by the force sensor and displacement sensors integrated into the Landmark 370 servo-hydraulic test system at a sampling frequency of 300 Hz. MATLAB 2019a is used to process experimental data and generate visual images in the manuscript. Through MATLAB 2019a, the mean values of voltage signals and force-displacement signals are obtained respectively to analyze the output characterization of the system.